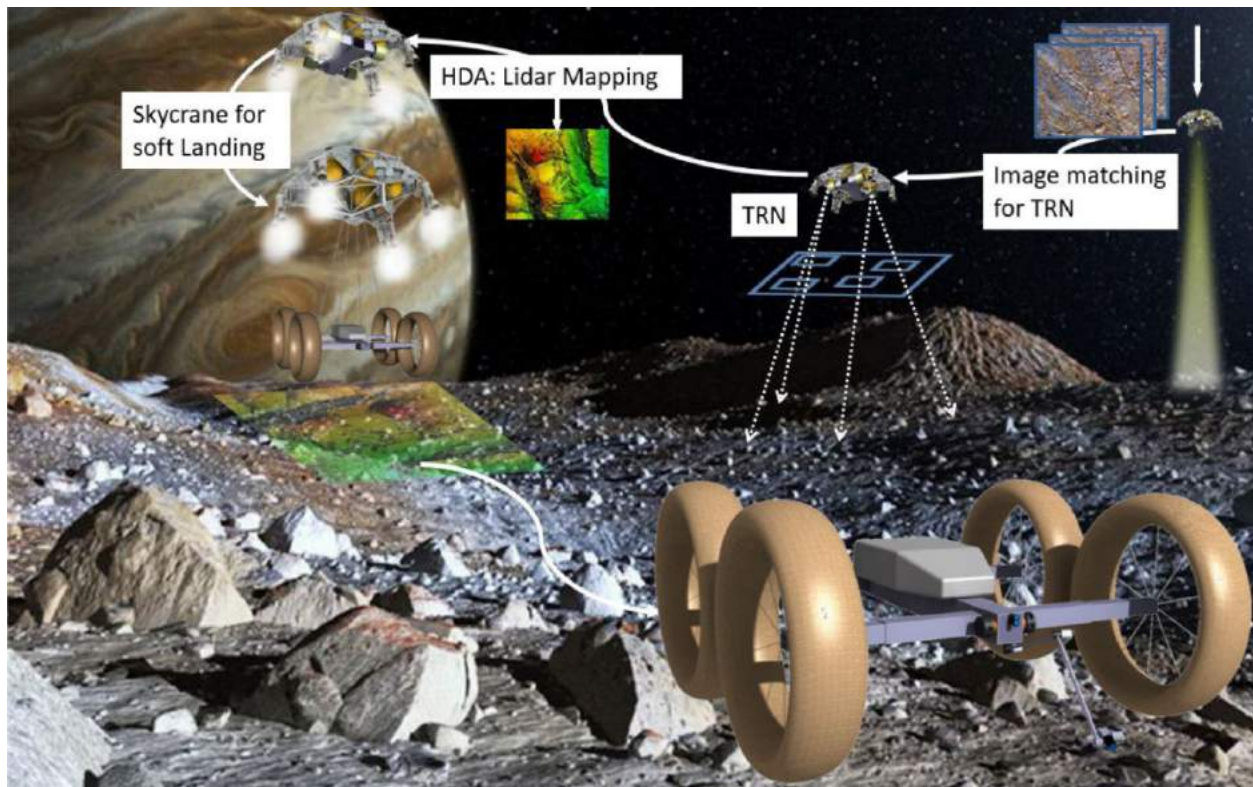# Advanced Spacecraft Technologies to Explore the Ocean Worlds for the Detection of Extant Life

Principal Investigator | Dr. James Longuski (Purdue University)

Co-Investigators | Dr. Sarag Saikia, Dr. Athul Girija

December 2021

PURDUE
UNIVERSITY.

School of Aeronautics and Astronautics, Purdue University

701 W. Stadium Ave.

West Lafayette, IN 47907

Advanced Spacecraft Technologies to Explore the Ocean Worlds for the Detection of Extant Life

Study Point of Contact

Dr. James Longuski

Professor

Purdue University

West Lafayette, IN 47907-2045

longuski@purdue.edu

Final Technical Report (August 2017 - November 2021)

December 19, 2021

Ocean World Single Wheel Test Rig Study Team

Purdue University

Dr. James Longuski (PI)

Dr. Sarag Saikia (Co-I)

Dr. Athul Pradeepkumar Girija

Dr. Ye Lu

Ms. Rachana Agrawal*

Mr. Archit Arora*

Thin Red Line Aerospace

Mr. Maxim de Jong

Smithers

Dr. Madhura Rajapakshe

Mr. Matt Kent

* Graduate Student

Contents

1. Executive Summary

This report provides an overview of a multi-year project in developing a single wheel test rig in support of the wheel design and testing for Ocean Worlds exploration. Design, assembly, and testing operation of the test rig are discussed and shown in details with key requirements including large diameter tire testing, reduced gravity test condition, flexible surface features, and flexible camber and slip angle settings. The design and fabrication of a prototype wheel and results from its preliminary testing are also discussed.

2. Introduction

Mobility systems have provided immense value in in-situ planetary exploration over the last five decades since Lunokhod-1, the first successful rover to operate on the lunar surface in 1970 [1, 2]. As opposed to orbital platforms which can only perform remote-sensing investigations and static landers which provide in-situ data but only for a single site, mobility systems enable in-situ measurements across a range of scientifically interesting sites. A wide range of mobility systems which include rovers, articulated robots, hoppers, helicopters, multicopters, balloons, airplanes, floating platforms, ice drills, and submersibles have been proposed for planetary exploration across the Solar System [3–12].

At the time of writing, NASA's Curiosity rover is operational on the Martian surface since 2012 and the Perseverance rover has been operational since 2021 [13, 14]. The European Space Agency's Rosalind Franklin rover is scheduled to arrive at Mars in 2022 [15]. The Chinese National Space Agency's Yutu 2 rover is operational on the lunar far side and has become the longest operational lunar rover, breaking Lunokhod-1's previous record of 10.5 months [16].

The continued interest and commitment in surface mobility systems despite their inherently higher costs compared to orbiter and lander missions underscore their importance in future planetary exploration. However, the poorly known surface properties and features (loose sand, large boulders, sharp rocks etc.) present significant engineering challenges to surface mobility systems. The most notable example is NASA's Spirit rover which became trapped in soft sand and could not gain traction to free itself, eventually leading to a loss of mission [17]. Prior to the embedding event, the Spirit rover had experienced significant slippage when crossing fine-grained surfaces [18]. The twin rover Opportunity has also been a subject to such near-embedding events as it traversed deformable sand terrain [19, 20]. Similar slippage and sinkage problems were encountered by the Curiosity rover when crossing ripple fields [21]; in addition to significant wheel damage from traversing over sharp rock outcrops [22]. These experiences make it clear that a thorough understanding of the wheel-soil/terrain interaction is of critical importance for planning future missions which include surface mobility systems. The Mars rovers used a combination of numerical modeling, single-wheel test rig experiments, and full vehicle field tests in analog sites such as the Mojave Desert to characterize the wheel-terrain interaction and predict vehicle performance. Based on the data, the operations teams select the best possible path so as to minimize the risk of undesirable events such as embedding in a sand trap.

While the majority of the existing literature in the field of planetary rovers focus on the Moon and Mars, the Ocean Worlds such as Europa and Enceladus in the outer Solar System are high-priority targets for in-situ exploration in the near future [23]. These Ocean Worlds are known to harbor massive liquid water oceans underneath their icy crust, and are prime candidates in the search of life beyond Earth [24]. Multiple studies have investigated the scientific potential and technical challenges of lander and mobile platforms on Europa and Enceladus [25–29]. Ocean Worlds such as Europa present a significantly more challenging environment compared to Mars due to the extremely cold temperature, high radiation dosage, and the poorly constrained material properties under these conditions. Preliminary studies using

photopolarimetric observations suggest that granular ice under cryogenic and vacuum conditions may be extremely fine grained material and is a potential hazard to landed spacecraft [30]. Other potential hazards include penitent-like formations which create sharp ice outcrops [31]; or massive boulder fields as seen by Cassini during close flybys of Enceladus [32]. We at Purdue University have developed a unique single wheel test rig to characterize wheel terrain interactions for future Ocean World mobility systems. The test-rig accommodates tires as large as 2 meters in diameter, and features a test-bed which can simulate varied surface features such as fine grained ice, smooth hard ice, sharp rock formations and boulder outcrops of a range of size distributions. This paper reports the design, capabilities, initial results and future applications of the Purdue Single Wheel Test Rig for Ocean World rovers.

3. Existing Single Wheel Test Rigs for Planetary Rovers

Understanding wheel-terrain interaction requires a combination of numerical models, theoretical methods, and experimental techniques. The single wheel test rig is an important element within the larger set of experimental techniques, and is often required to validate the terramechanics models as well as provide empirical relationships for use in these models. Numerous single-wheel test rigs have been developed by universities and other institutes to characterize wheel-terrain interaction in support of planetary missions. This section provides a brief overview of a selected set of existing single-wheel test rigs and their capabilities.

Figure 1(a) shows the Massachusetts Institute of Technology (MIT) single wheel test rig used in support of the testing for the Curiosity rover operations on the Martian surface. The test rig allows control of the wheel slip ratio and the vertical load and measures the traction force, driving torque, and wheel sinkage in Mars simulant soil [33]. Figure 1(b) shows the Carnegie Mellon University (CMU) single wheel soil imaging test bed also used in support of the Curiosity rover. The CMU test rig provides a unique imaging analysis capability of soil motion at and below the wheel-soil interface [34]. Figure 1(c) shows the Rover Chassis Evaluation Tool (RCET) single wheel test rig built at the German Aerospace Center (DLR) in support of the ExoMars rover project [35]. Figure 1(d) shows the single wheel test bed at Tohuku University designed to support Japanese lunar exploration missions. In addition to the vertical load and slip ratio, the test rig allows control of the slip angle for the experiments [36]. Figure 1(e) shows the single wheel test rig at Politecnico di Torino built in support of the AMALIA lunar rover mission [37], and features slip and camber angle control during the test [38]. Figure 1(f) shows the wheel-soil interaction test bed at Harbin Institute of Technology (HIT) in support of lunar exploration programs. Table 1 summarizes the key characteristics and test capabilities of the various single wheel test rigs described in this section, and are compared to the proposed Purdue single wheel test rig for Ocean World rovers. More extensive reviews of both computational and experimental techniques for planetary wheel-soil interaction are presented by in numerous review articles in the literature [39–41].
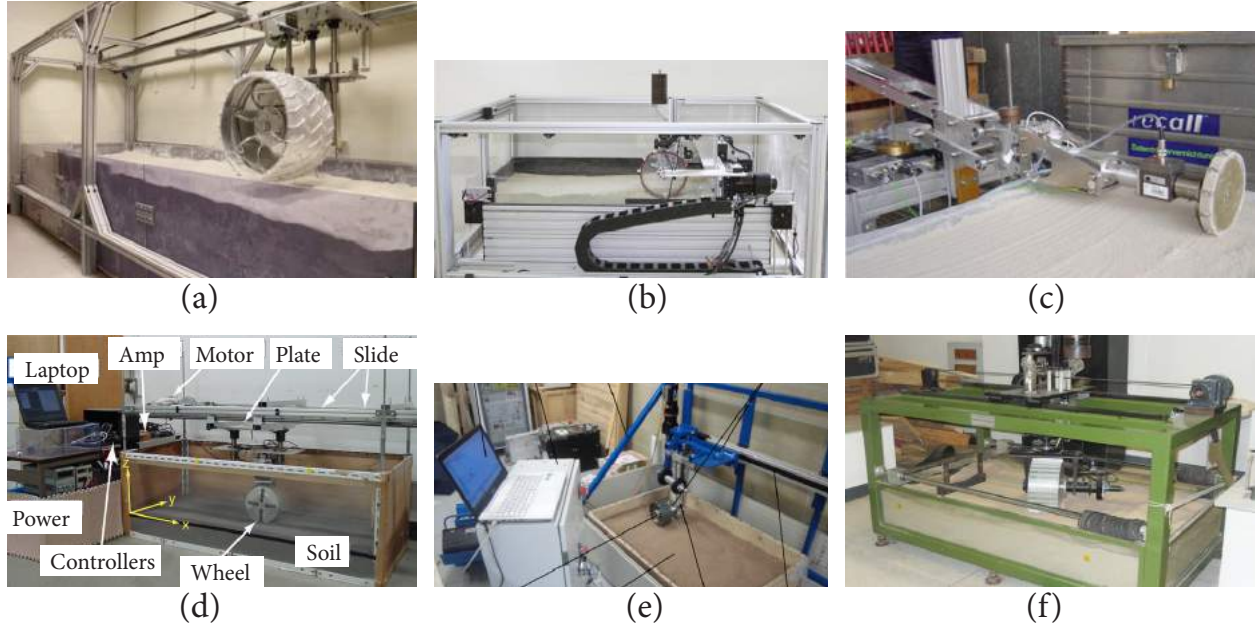
Fig. 1 **Existing single-wheel test rigs at various academic and research institutions. (a) MIT Single Wheel Test Rig [33]; (b) CMU Single Wheel Soil Imaging Testbed [34]; (c) ESA ExoMars Project Single Wheel Test Rig [35]; (d) Tohuku University Single Wheel Test Bed [36]; (e) Politecnico di Torino Single Wheel Test Rig [38]; (f) HIT Wheel-Soil Interaction Test Bed [42]**

Table 1 **Summary of key characteristics and capabilities of the various single wheel test rigs**

	Length m	Speed mm/s	Tire diameter, cm	Slip ratio control	Slip angle control	Camber angle control	Dynamic load control
MIT	3.5	60	50	✓	✗	✗	✗
CMU	1.0[a]	1.0	50	✓	✗	✗	✗
ESA RCET	3.0[a]	n/a[b]	25	✓	n/a[b]	n/a[b]	✗
Tohuku	2.0	35	20	✓	✓	✗	✗
Torino	2.7	n/a[b]	18	✓	✓	✓	✗
HIT	1.7	n/a[b]	40	✓	✓	✗	✗
Purdue [c]	4.8	200	200	✓	✓	✓	✓

[a] Estimated by the authors
[b] Data not available

4. Design and Fabrication of the Single Wheel Test Rig

The high-level objectives of the work described in this paper are as follows: 1) Design and construction of a single wheel test rig for Ocean World rovers, 2) Construction of a prototype novel large-diameter deployable rover wheel, and 3) Demonstrate the test rig capabilities using the prototype wheel under a range of slip ratios and other test conditions expected on Ocean World surfaces. The requirements for the test rig are derived from these high-level objectives, and are described in the following subsections. Section 5 provides a detailed description of the design, fabrication, and design rationale of the prototype wheel.

A. System Requirements and Constraints

The overall rig design is driven by the requirement to accommodate the prototype test tire which is approximately 1 meter in diameter and 25 cm in width. During the early stage of the design, the choice between using a horizontally moving surface with the wheel held in place was considered, as opposed to a static surface on which the wheel will be rolled over. While a moving underlying surface is ideally suited for flat surfaces and is widely used in the automobile industry for dynamic wheel testing, it presents inherent difficulties when flexibility is required in terms of the nature of the surface. To accommodate a wide range of surface features such as granular ice and boulder fields, it was decided to use a horizontally moving wheel over a static test bed which can be reconfigured with different surface conditions.

The length of the test-rig is driven by an empirical rule that the test should run for at least one wheel revolution to accommodate startup transients before the wheel reaches the desired slip conditions. This imposed a requirement of at least 3.5 meters of usable test bed length. The maximum allowable footprint (due to space constraints) of the test rig footprint was 6.0 meters. Considering these constraints, the test rig is 6 m × 2 m × 2 m (length × width × height), and provides 4.5 meters of usable test bed length.

The next major requirement is to be able to test the prototype wheel under a range of slip ratios. The wheel slip ratio s is a non-dimensional parameter defined as follows [36].

$$s = \begin{cases} (r\omega - v_x)/r\omega & \text{if } |r\omega| > v_x, \text{positive slip} \\ (r\omega - v_x)/v_x & \text{if } |r\omega| < v_x, \text{negative slip} \end{cases} \tag{1}$$

where r is the wheel radius, ω is the wheel angular speed, and v_x is the wheel horizontal speed. A desired slip ratio is achieved by providing independent control of both the wheel angular speed and the wheel horizontal speed. Planetary rovers typically operate at very low speeds (< 0.1 m/s), and hence most existing single wheel test rigs are designed to operate at such speeds as seen in Table 1. Figure 2 shows the required wheel angular speed as a function of the wheel horizontal speed for a range of slip ratios. Ideally, the test rig should be capable of accommodating the entire theoretical range of slip ratios for any given horizontal speed. However, as seen in Figure 2, this is not realizable as the required angular velocity increases sharply as the slip ratio approaches 1.0. The selected operating range for ω and v_x are shown in green in Fig. 2 which allows slip ratios as high as 0.8 for a nominal horizontal speed of 0.1 m/s. The upper limit for v_x of 0.2 m/s is an arbitrary design requirement based on the expected speed of a future planetary rover, and to achieve negative slip values with reasonably large ω (> 0.2 rad/s) as shown in Fig. 2.

The vertical load on the wheel F_v is another important test parameter, and must be controlled to simulate the wheel-soil interaction on planetary surfaces with different values of surface gravity. The prototype test wheel is intended to be used on a 4-wheel rover weighing approximately 800 kg which will be delivered to Europa's surface using an MSL-derived skycrane descent system. Taking into account Europa's surface gravity of 1.32 m/s^2, this results in a
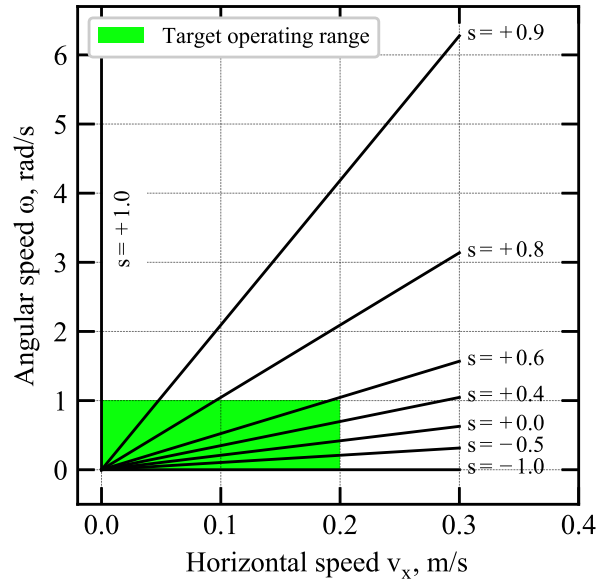
Fig. 2   Required wheel angular speed as a function of horizontal travel speed at various slip ratios (for the prototype test wheel with diameter = 0.956 m)

vertical load of 264 N for each wheel. The corresponding loads on Mars, Titan, and Enceladus are 744 N, 270 N and 22 N respectively. If the vehicle is moving up or down a slope, the local vertical component of the force will be smaller as defined by the slope angle. Considering these loads, the requirement for the vertical load on the wheel is in the range of 20–400 N. The nominal load accuracy requirement is arbitrarily set to 1% of the desired value, though this may not be practical at very low vertical loads (i.e., << 20 N).

The requirements for slip angle α and camber angle β (as illustrated in Fig. 3) are both arbitrarily defined at ±25 degrees, which is a nominal upper bound for the range of these angles expected for planetary rovers. The test bed needs to accommodate the prototype 25-cm wide wheel in the slip and camber angle geometries, and is required to be at least 70 cm wide and 30 cm deep. The test bed is required to be able to be simulate a wide range of conditions which may be expected on icy moons such as Europa. Figure 4 shows some of the highest resolution photographs of Europa and Enceladus from the Galileo and Cassini-Huygens spacecraft. As a starting point the test bed is required to able to accommodate granular ice simulant, boulder fields, sharp ice formations and also provide a flat hard surface resembling smooth ice. Laboratory studies using both observational data from spacecraft and telescopes, experimental studies of water ice under cryogenic and vacuum conditions are currently underway. Analog sites such as the ones shown in Fig. 5 may offer some insight into the conditions on these icy worlds, though ice is known to behave very differently under cryogenic conditions than that encountered on Earth. As more data becomes available, other test bed simulants and surface features may be used to provide more realistic representation of the icy moon surfaces.

The most important measurements of interest are the forces and moments on the wheel as it rolls across the surface
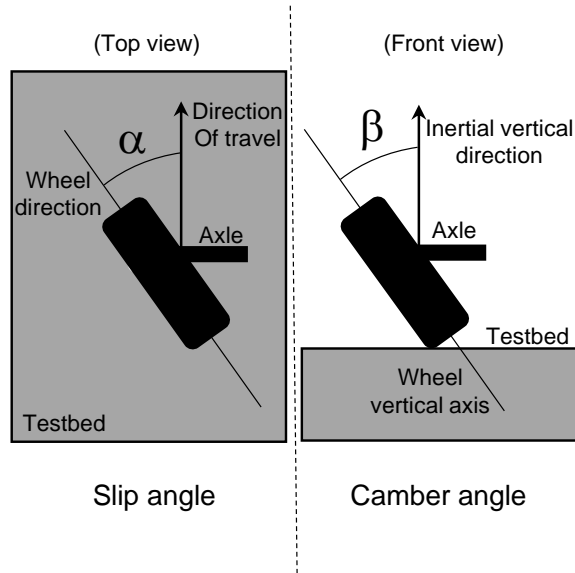
5

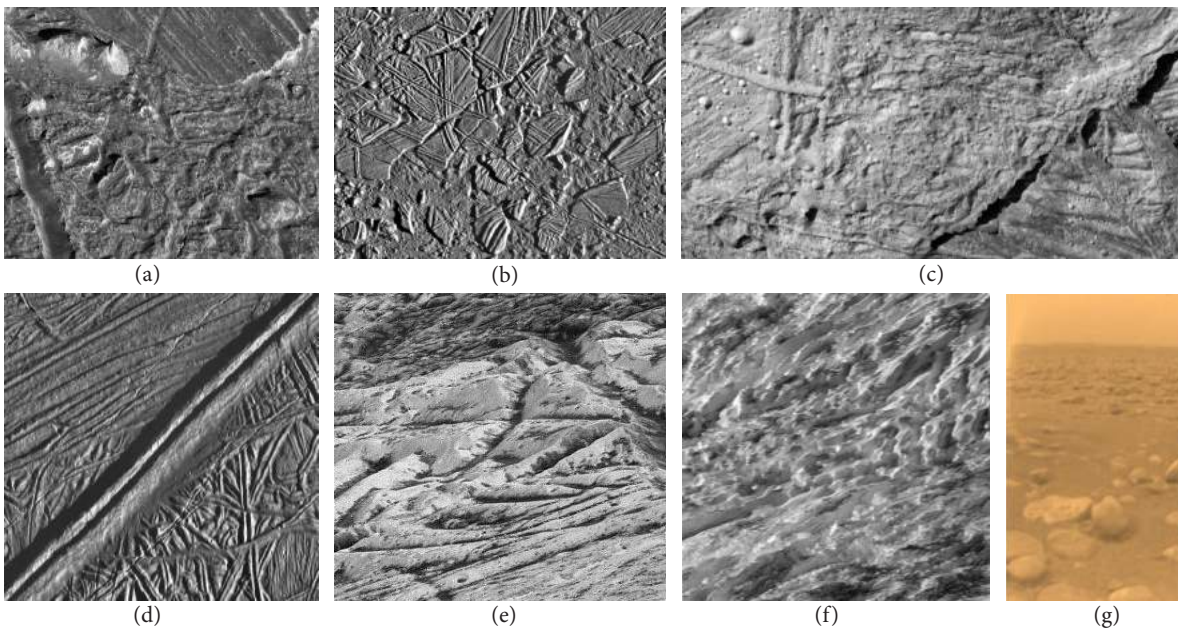**Fig. 3 Schematic illustrating slip and camber angles.**

Fig. 4 High resolution images showing the varied surface features on Ocean Worlds. (a) Very high resolution view of the Conamara Chaos on Europa. The image is 5 km wide and shows a rugged surface with ice blocks that have been broken up and then frozen. Credit: NASA/JPL/PIA01177. (b) High resolution image of Europa's jumbled crustal plates, showing an area 42 km wide. Credit: NASA/JPL/PIA00591. (c) High resolution image of Europa' surface showing numerous impact craters amid rugged terrain, image is 8 km wide. Credit: NASA/JPL/PIA01404. (d) Close-up image of one of Europa's ubiquitous double ridges. The ridge is 2.6 km wide and rises to about 300 m. Credit: NASA/JPL/PIA00589. (e) Highest resolution image of Europa showing an area 1.8 km wide. Credit: NASA/JPL/PIA01180. (f) Close-up view of Enceladus, showing an area 7.6 km wide. Credit: NASA/JPL/PIA17204. (g) Titan's surface as seen by the Huygens probe showing pebble-sized ice blocks about 15 cm across. Credit: NASA/JPL/ESA/PIA07232.

(a)　　　　　　　(b)　　　　　　　(c)
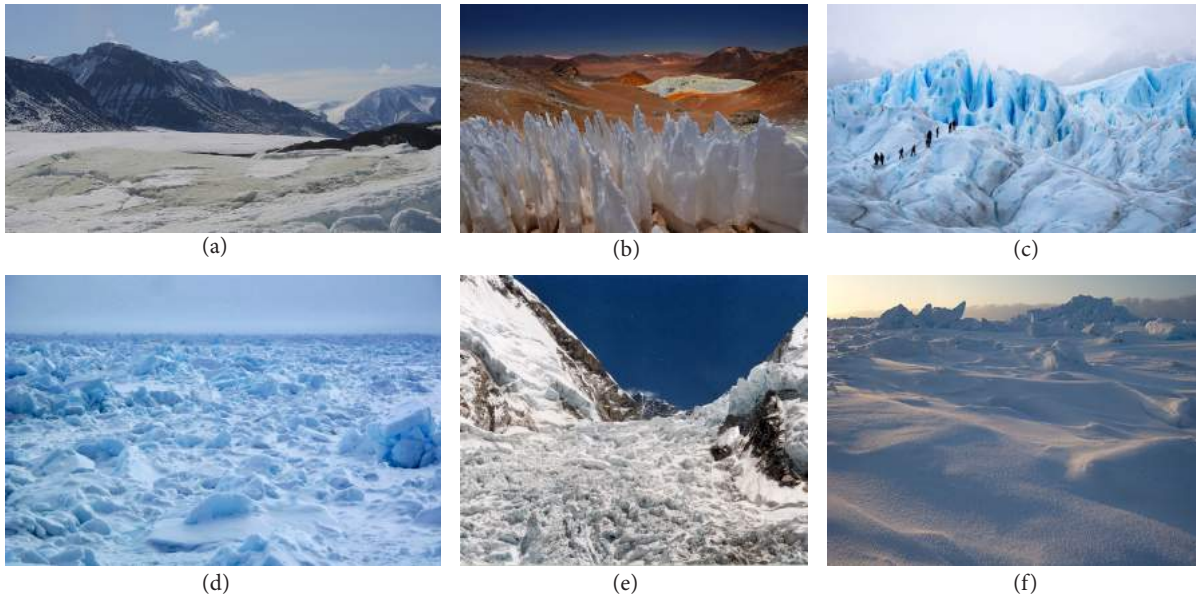
(d)　　　　　　　(e)　　　　　　　(f)

Fig. 5   Various ice formations on Earth, some of which may be representative of the landscapes on icy moons such as Europa and Enceladus. (a) Sulfidic outcrop (yellow colored marking on the ice) in Borup Fiord Pass glacier, Ellesmere Island in the Canadian High Arctic. A sulfur-rich spring passes under glacial ice before emerging onto the surface, making it one of the most interesting Earth-analog sites for Europa from an astrobiological perspective. Whether it presents an analog for the terrain is currently not known, but relatively smooth and flat terrain is likely present at some locations on Europa, and will be attractive landing sites from a safety perspective. Credit: NASA Astrobiology Website, John Spear at the Colorado School of Mines. (b) Penitentes on the Cerro Toco volcano in the Atacama Desert in Chile. Such sharp ice features formed in dry high altitude are formed by differential ablation and are known to reach several meters in height. penitentes have been discovered on Pluto [43], and may be present at Europa at some latitudes [31]. Credit: Federico Ce, www.trekearth.com. (c) Extremely rugged ice formations in the Perito Moreno Glacier in Argentina, note the people for scale. Such terrain is likely present on icy moons and presents formidable challenges for mobility systems, though non-conventional systems such as snake-like robots may be more suited than wheeled rovers. Credit: www.macdermottsargentina.com. (d) Sea ice floating off the coast north of Barrow, Alaska. Credit: Ned Rozell/University of Alaska, Fairbanks. (e) Jumbled up ice blocks each several tens of meters to a few meters in size at the Khumbu Icefall in Nepal en-route to Mt. Everest. Sites such as the Conamara Chaos on Europa which shows activity of relatively recent (in geologic timescales) interaction with the underlying liquid water ocean will likely feature such extremely rugged terrain. Credit: Uwe Gille, Wikipedia, CC-BY-SA-3.0. (f) Powdery snow on sea ice near Barrow, Alaska. Credit: Chris Linder/University of Washington. Such terrain is likely present at Enceladus' south polar regions from freshly fallen material ejected from the active geysers [32], and may present a hazard for landers and rovers which may sink into the surface.

under different test conditions, and is accomplished using 6-axis Force Torque (FT) sensor. Figure 6 shows the wheel coordinate system centered at the wheel hub and the definition of the drawbar pull F_X, lateral force F_Y, normal force F_Z, lateral rolling moment M_X, drive torque M_Y, and the aligning torque M_Z. Wheel displacement in the vertical direction is required to measure sinkage, and along the horizontal direction to measure wheel slippage. A LabVIEW program is developed to set the various test parameters (horizontal traverse speed, wheel rotational speed, vertical load, slip angle, camber angle) and record the measurements (wheel forces and torques, vertical and horizontal displacement).
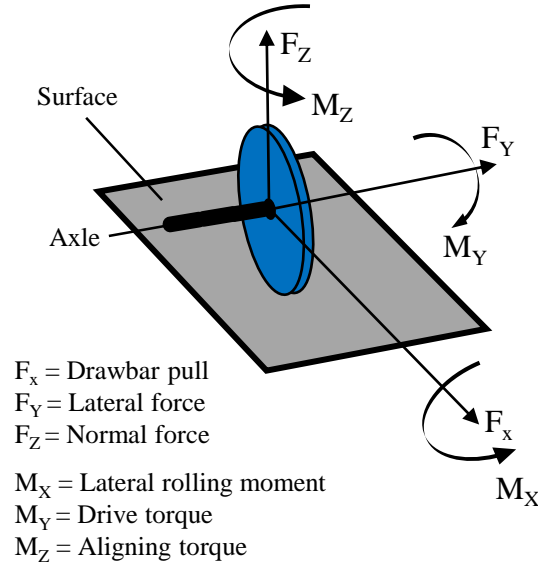
F_x = Drawbar pull
F_Y = Lateral force
F_Z = Normal force

M_X = Lateral rolling moment
M_Y = Drive torque
M_Z = Aligning torque

Fig. 6   Wheel forces and moments.

B. Mechanical System Design

The test rig mechanical system consists of the following subsystems as shown in Figure 7: main structure, horizontal motion control, vertical motion and load control, slip and camber angle control, wheel drive, and simulant bed. Details of the each mechanical subsystems and their construction are given below.

1. Main Structure and Horizontal Motion Control

The main structure is made of standard slotted aluminum extrusions and is 6 meters long, 2 meters wide, and 2 meters high as shown in Figure 8(a). Horizontal motion control is achieved using a carriage supported on wheels as shown in Figure 8(b). The carriage is the primary moving structure and supports the various subsystems below including the vertical load control and the wheel drive mechanism, all of which move along with the carriage. The carriage is driven using a pulley and timing belt, which is connected to a motor as seen in Figure 8(c). The top of the frame serves as a guide rail for the carriage as it moves horizontally. By controlling the speed of the drive motor, the horizontal traverse speed of the wheel can be set to the desired value.

2. Vertical Motion and Load Control

The main goal of the vertical motion and load control system is to control vertical force on the wheel, in particular to offload, to simulate its motion on reduced-gravity environments such as those encountered at Europa and Enceladus. The entire wheel assembly is supported on rollers as shown in Figure 9(a, b), and can move in the vertical direction. The load control is achieved using a linear actuator and an extension spring. The linear actuator controls the tension on the spring hence changes the forces transmitted to the wheel by the system weight. The desired vertical load is set by a
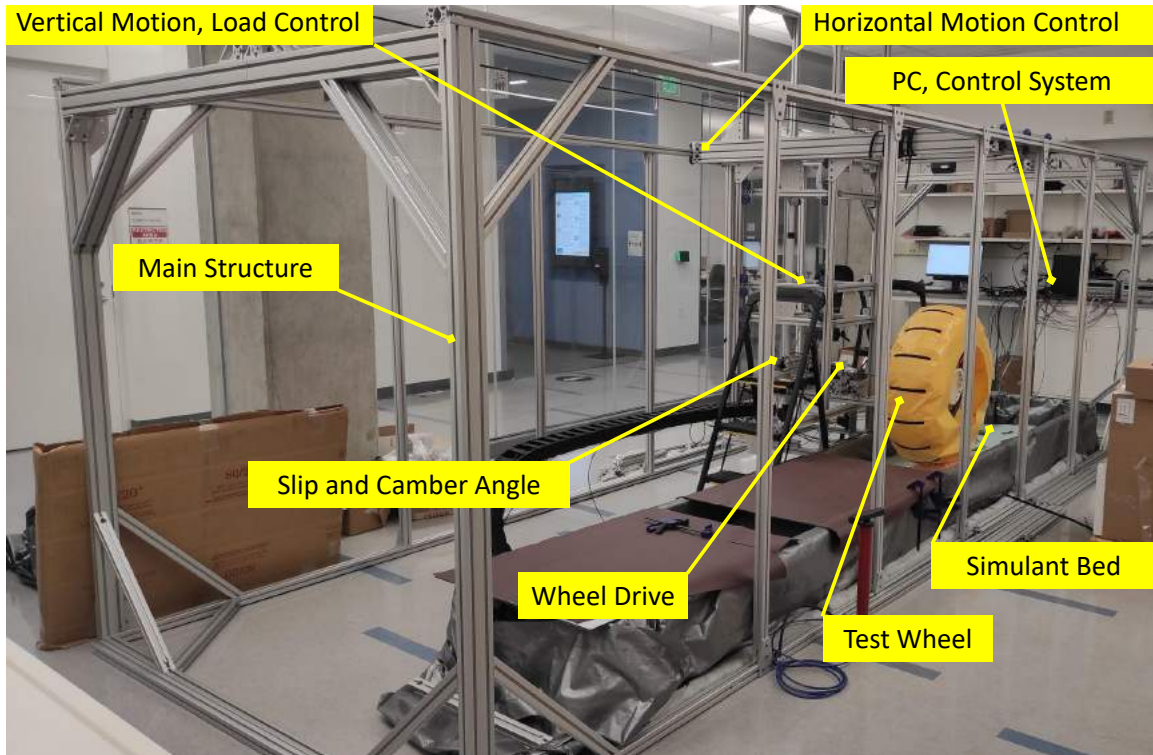
8

Fig. 7   Purdue single wheel ocean world test rig.

feedback-loop control of the length of the extension spring using the linear actuator. A single-axis load cell as shown in Figure 9(c), will measure the vertical load on the wheel for the feedback loop.

3. Slip and Camber Angle Control

The slip and camber angle control system allows setting desired slip and camber angles at the beginning of a test. The range of achievable angles is roughly ±30° for both slip and camber. Slip and camber control is achieved using a linear actuator and a gear motor as shown in Figure 9(a). The slip mechanism consists of a linear actuator that changes the angular position (i.e., slip angle) of the wheel-motor assembly arm. The actuator extends out to rotate the wheel counter-clockwise about the vertical axis (Z-axis) as shown in Figure 9(a). The camber mechanism consists of a servo motor-gear system that can move the wheel-motor assembly about the traverse axis (X-axis). An inclinometer attached to the wheel-motor assembly rod measures the camber angle. Figure 10(c,d) illustrates the slip and camber angle control systems in use during tests. The current systems only allow static slip and camber angle testing, since testing with dynamic slip and camber angle requires a constant contact patch between the wheel and surface which are more complicated to implement and will require more degrees-of-freedom on the wheel motor assembly.
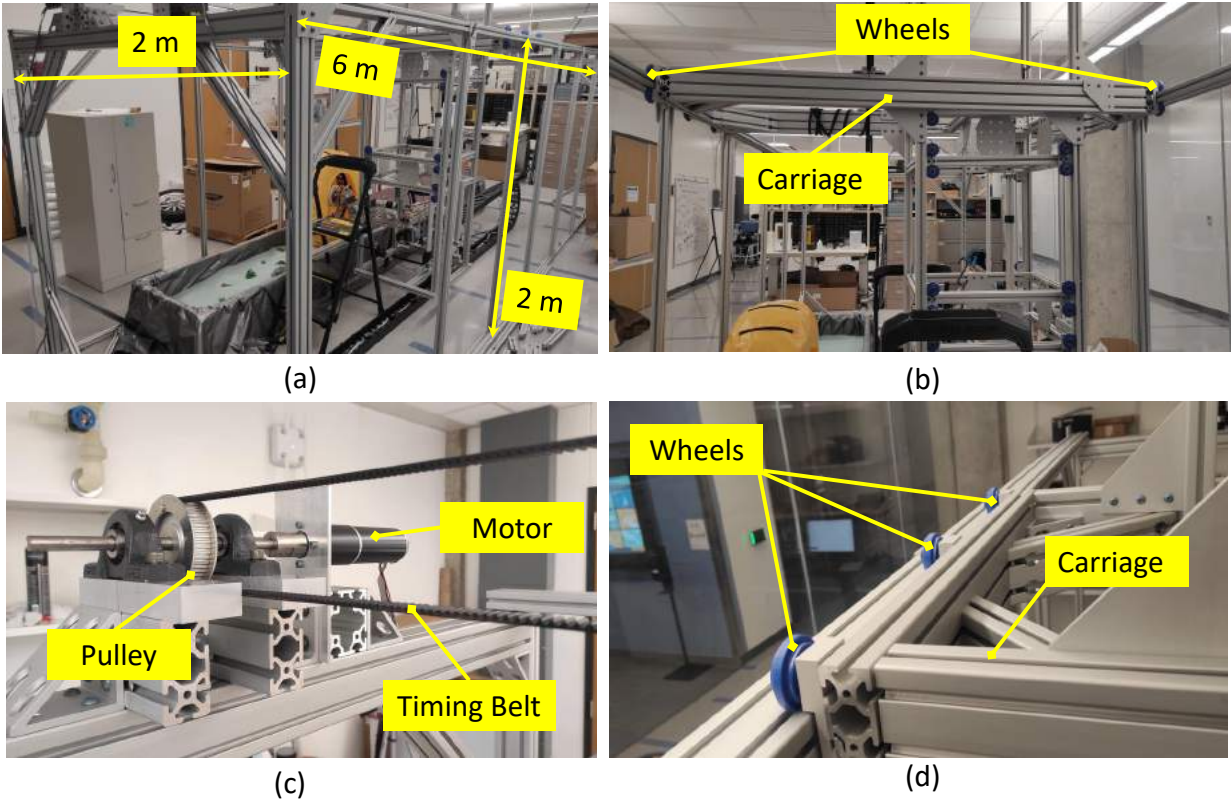
9

Fig. 8 **Main structure and horizontal motion control. (a) Dimensions of the main structure. (b) Carriage for horizontal motion, and carriage wheels which move along the main structure. (c) Carriage drive system using a pulley, timing belt, and drive motor. (d) Close-up view of carriage wheels on the guide rails.**

4. Wheel Drive

The test wheel is driven using a DC motor as shown in Figure 10(a). A six-axis FT sensor is mounted between the test wheel and the mounting adapter plate to measure the reaction force and torque. Figure 10(b) shows the assembled wheel motor drive on the simulant test bed with zero slip and zero camber angle. Figure 10(c) shows the wheel at a non-zero slip angle and zero camber angle during a test. Figure 10(d) shows the wheel at zero slip angle and a non-zero camber angle prior to a test.

5. Simulant Bed

The simulant test bed is designed to accommodate a wide range of surface conditions expected on Ocean World surfaces. Figure 11(a) shows a flat rough surface created using sandpaper (laid on top of a metal plate). Figure 11(b) shows a flat smooth surface created using a polycarbonate panel. Figure 11(c) shows the tire on a snow simulant (fine glass bubbles). Figure 11(d) shows the tire in a simulated ice boulder field.
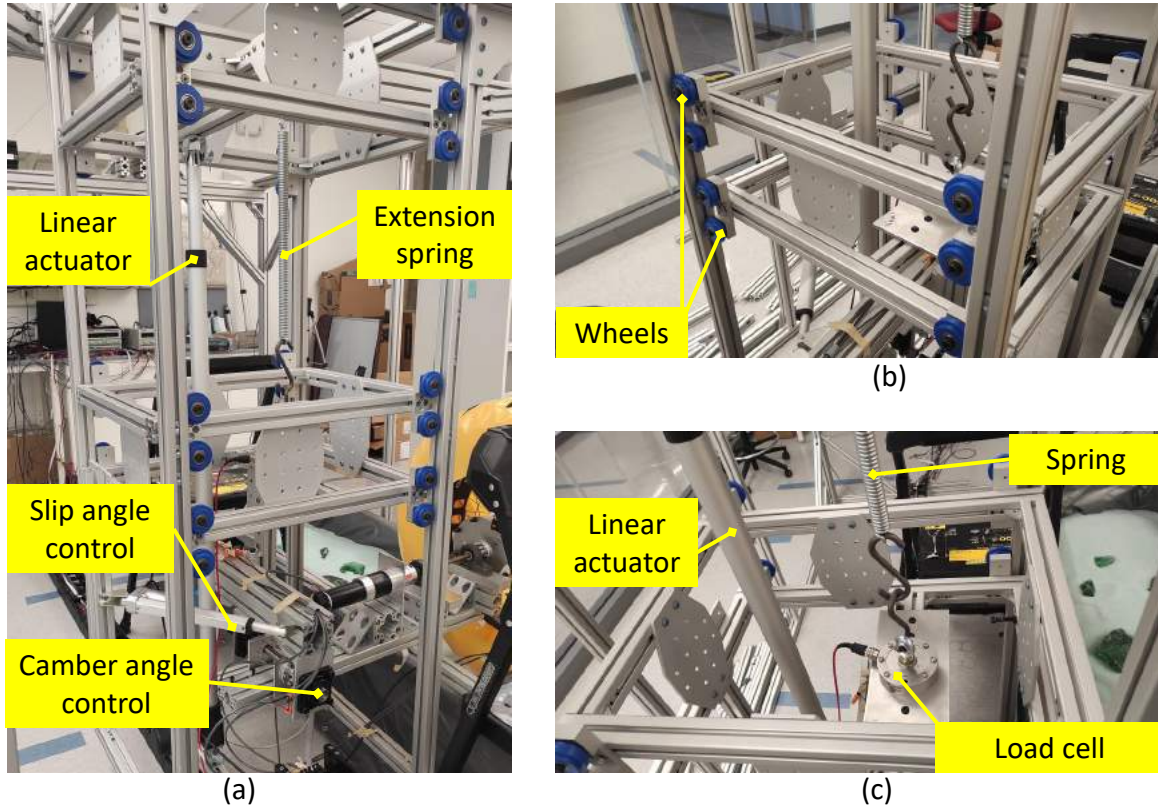
Fig. 9   Vertical Motion and Load Control. (a) Linear actuator and extension spring used for vertical load control. (b) Rollers for vertical motion. (c) Load cell for measuring the vertical force on the whee.

C. Electrical and Control System Design

The electrical components, including wheel motor, slip and camber actuators and the sensors are attached to the moving carriage frame. Thus majority of the electrical sub-system moves back and forth across a 5 meter long track. All the cables from instruments on the carriage are routed through an energy chain system that allows a guided motion of the cables. The motors are controlled through individual motor controllers that receive command from the computer. The sensors send the signal to the computer through the National Instrument data acquisition input/output device. All instruments are powered through two DC power supplies. Figure 15 shows the schematics of the electrical subsystem.

The test rig has a number of sensors that ensure the proper operation under the desired testing condition. All sensors and actuators are selected for the initial setup of the test rig. Based on the specific applications, most of the sensors and actuators can be changed easily with different specifications.

1. Actuators

The test rig uses a total of five actuators: three motors for horizontal carriage motion, wheel driver, and camber mechanism, and two linear actuators for vertical load control and slip mechanism. The carriage motor and wheel motor combined provides full control over the wheel motion and both are the Maxon RE 50 DC motors rated at 200 W. The
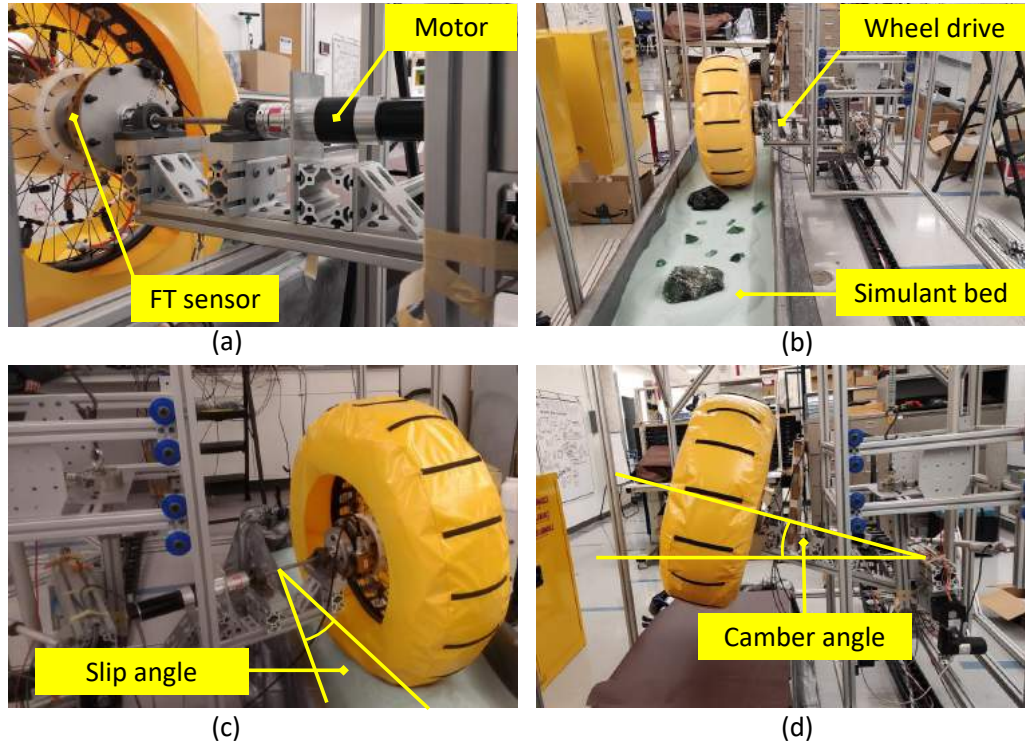
11

Fig. 10 Wheel drive. (a) Drive motor and FT-sensor placement. (b) Zero slip and zero camber angle. (c) Non-zero slip angle and zero camber angle. (d) Zero slip angle and a non-zero camber angle.

carriage motor is paired with Maxon reduction gear GP 52 C with reduction ratio of 126:1, and the wheel motor is paired with Maxon GP 62 A with a reduction ratio of 236:1 to provide the necessary torque and speed. The camber motor requires a high torque to stabilize the long drive arm, and a high torque stepper motor from Anaheim Automation is used with 100:1 gear to provide a precise control over the camber angle. Both linear actuators are from Progressive Automation. The linear actuator for the load control is the model PA-04 capable of a maximum stroke length of 1 m and a maximum dynamic and static load of 1800 N. For slip angle control, we used the model PA-14 with maximum dynamic and static forces of 680 N and 1560 N respectively with a stroke length of 0.2 m.

2. Sensors

Six-axis force and torque sensor is a key component of the test rig which directly measures the three-axis forces and torques from the wheel. Given the large wheel diameter, the selected FT sensor is the ATI Omega-160 (DAQ version) with maximum measurable single axis force of 6250 N and 2500 N along axial and longitudinal directions respectively, and maximum measurable single axis torque of 400 N-m in all axes. Single-axis load cell is used to achieve active load control. Considering the weight of the drive, vertical motion, and camber and slip structures, the load cell is the FUTEK LCF450 that measures up to 1300 N.

Two draw-wire sensors measures the horizontal carriage displacement and vertical wheel displacement. The
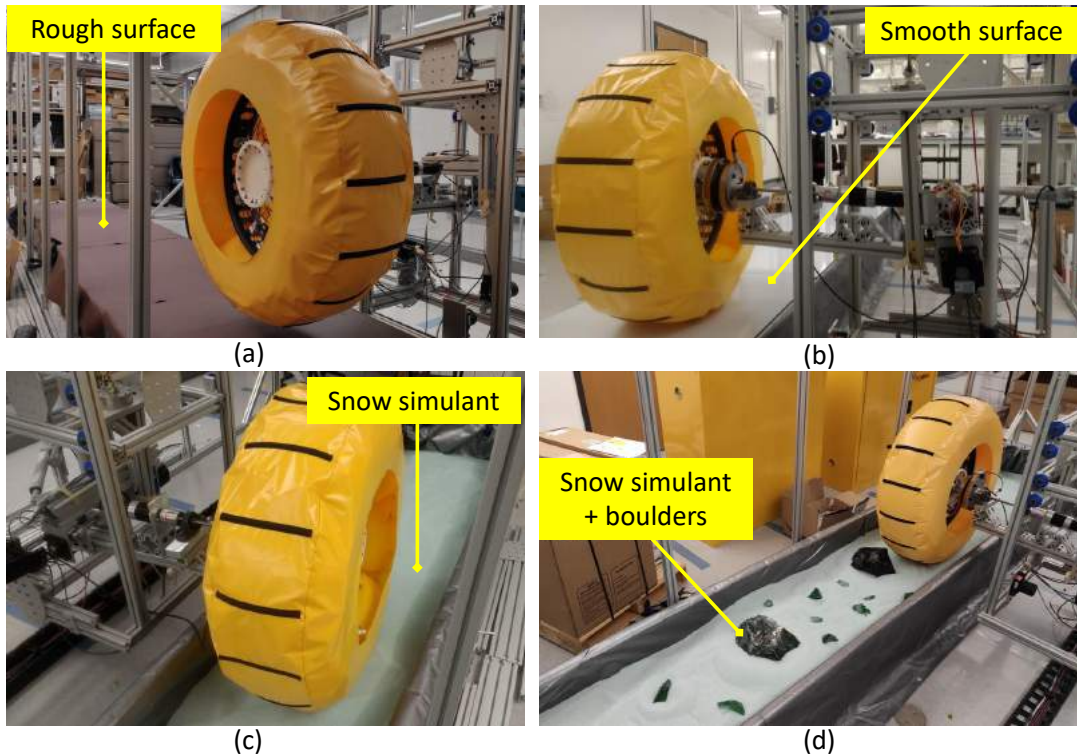
12

Fig. 11 Reconfigurable simulant bed which can simulate a wide range of surfaces which might be encountered on Ocean Worlds. (a) Flat rough surface created using sandpaper (laid on top of a metal plate). (b)Flat smooth surface created using a polycarbonate panel. (c) Snow simulant (fine glass bubbles). (d) Simulated ice boulder field.

horizontal system uses the Micro-Epsilon WDS-P115 sensor with measuring range of 7.5 m to provide the full range measurement. The vertical system uses the Micro-Epsilon WPS-MK88 model with a measuring range of 2.3 m, which serves as a redundant unit for load control (in addition to the single axis-load cell) since the primary load offset is achieved with a linear tension spring. The vertical draw-wire sensor can also provide measurement of the wheel vertical motion that can then be to used to characterize the tire motion and deformation over over different surface features.

The slip angles is measured using a rotary encoder (model ERCF 1) from P3 America and the camber angle is measured using an inclinometer from TTI Americas. The slip angle is a relative measurement therefore it needs to be calibrated using flatbed surface before the test. Each drive motor comes with an integrated encoder that measures the rotational speed of the motor.

D. Software Interface

The force and torque sensor and the National Instrument data acquisition input/output device (which interfaces all of the other sensors and actuators) are directly wired to the desktop machine and the test rig operator interfaces with these systems using the Laboratory Virtual Instrument Engineering Workbench (LabVIEW) software package.

The force and torque sensor comes pre-packaged with a LabVIEW program to obtain the raw voltage inputs and

convert them into the desired forces and torques, using a manufacture-provided calibration matrix. This program comes with the built-in functionality to record data at a desired sample rate that is output to a simple CSV file. This software program is shown in Fig. 12 and is used as the basis for all data collection for the test rig.
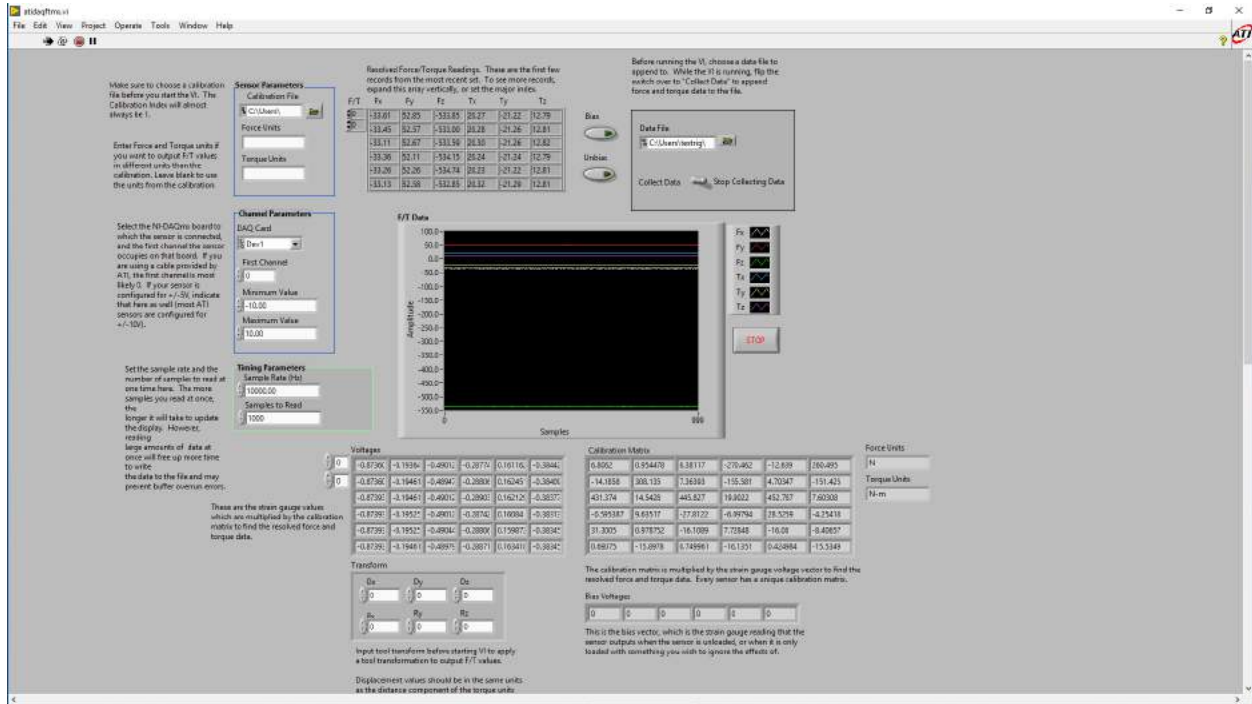

Fig. 12   Pre-packaged LabVIEW program for the force and torque sensor.

This base program is further enhanced to facilitate the simultaneous recording of all other sensor data from the data acquisition system during the primary data collection from the force and torque sensor. The enhanced program allows the operator to view both the raw and calibrated data (if available) from all sensors connected to the primary data acquisition system in addition to the force and torque data, and when data collection starts all of the sensor data is recorded, as shown in Fig. 13.

In addition to the data collection program, several other LabVIEW programs are used to control the different actuators and motors, as shown in Fig. 14.

5. Prototype Wheel Fabrication

Figure 16 shows the state-of-the-art in planetary rovers that are currently operational on the Martian surface. The MSL tires are machined from solid blocks of aluminium and are 50 centimeters in diameter and 40 centimeters wide [44]. The tires sustained damage under stress levels due to ventifacts (sharp wind-eroded rock formations cemented into the ground) that were not expected and hence were not tested for [45]. The design was modified for the Mars 2020 rover, with slightly larger diameter, smaller width, and increased thickness to improve robustness. The number of treads on
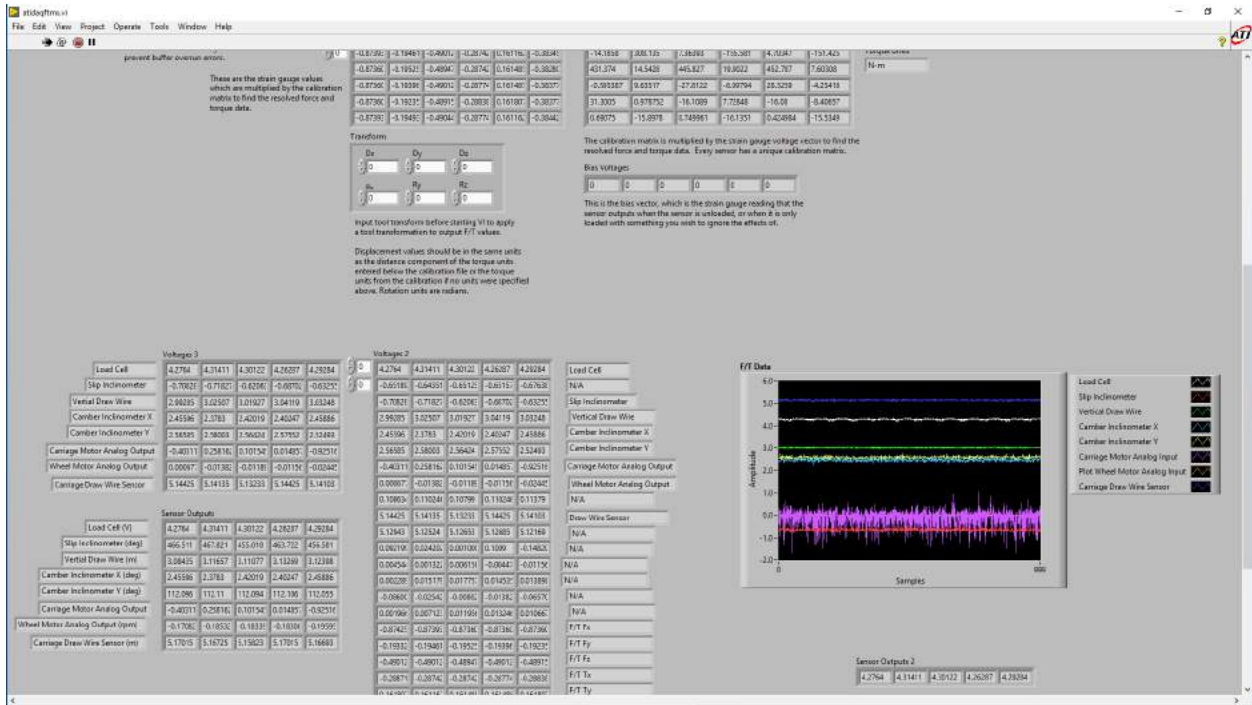
Fig. 13 Enhanced program that allows for the viewing and recording of all data acquisition sensor data in addition to the force and torque data.
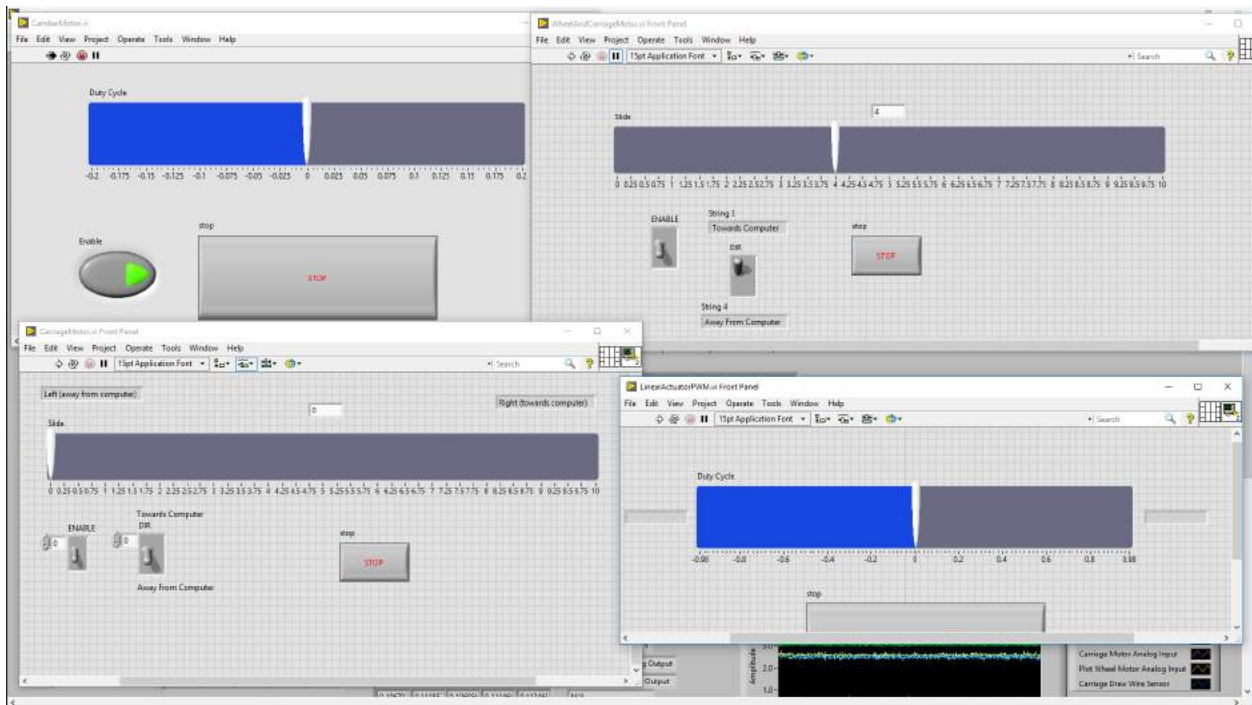

Fig. 14 LabVIEW programs to allow the operator to control the different actuators and motors that make up the test rig.
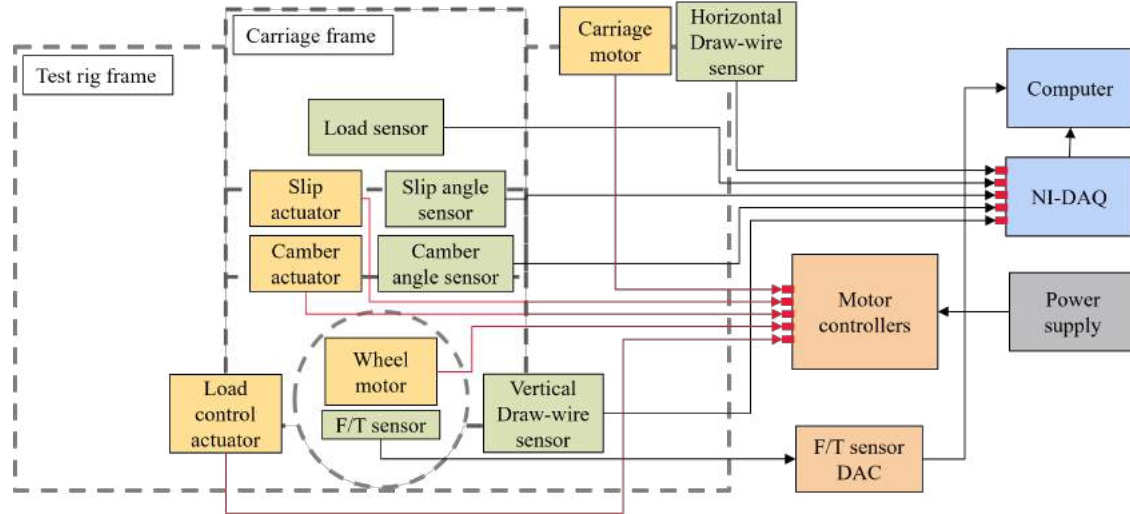
Fig. 15 Block diagram of electrical subsystem. Green - sensors. Yellow - actuators.

the rim are doubled and have a sinusoidal curve over the W-shaped pattern of MSL tires [46]. Rovers sent to Ocean Worlds such as Europa may encounter much more jagged terrain and sharp ice and rock formations. In contrast to the conventional rigid metal wheel used on Mars rovers, we propose a novel flexible tire concept which is more suited for such extreme terrain mobility.

Fig. 16 State of the art in rover wheels at NASA. (a) The left middle wheel of MSL rover image taken by Mars Hand Lens Imager (MAHLI) of MSL. The holes on tire surface and broken tread on top are conspicuous. Credit: NASA/JPL/PIA21486. (b) Mars 2020 rover wheel with increased tread count and modified curvature. Credit: NASA/JPL/PIA23269. (c) The "Spring Tire" made from nickel titanium SMA undergoing durability testing in simulated Mars terrain at JPL. Credit: NASA/Imaging Technology Center at NASA Glenn.

NASA Glenn Research Center has been developing nickel titanium shape memory alloy (SMA) tires for exploration rovers on Moon and Mars which would conform to irregular surfaces without sustaining damage (Figure 16 (c)).

16

A. Wheel requirements

The rugged terrain, variety in surface features, cold environment leads to following requirements from the tire that are addressed in the design of the novel tire concept for Ocean Worlds:

- **Large diameter**: The size of obstacles that a rover can surmount is primarily a function of suspension system and the wheel diameter. The rocker-bogie design used by the Mars rovers allows the rover to go over obstacles that are upto about twice the wheel diameter. However, the rocker-bogie suspension system is mechanically complex, limits the traverse speed, and presents challenges in extremely cold environments where the actuators must be kept warm and lubricated. This study proposes to use a mechanically simpler four-wheel drive vehicle such as that used by the Lunar Roving Vehicle where all moving parts can be housed inside the main chassis, and hence avoid problems with lubrication in extremely cold environments. However, such vehicles can only overcome obstacles that are about half the diameter of the wheels. To make up for this limitation of the four-wheel design, it is proposed to use large diameter wheels (> 1 meter) to overcome obstacles up to 0.5m.

- **Deployable**: Large diameter wheels present inherent difficulty for packaging onboard the delivery spacecraft, aeroshell, and launch vehicle fairing. The proposed wheel design will be stowed in a compact configuration during launch and cruise, and will be deployed to its final configuration just before touchdown during the sky crane maneuver.

- **Conformable**: Compared to rigid tires used on the Mars rovers, the proposed tire will conform to the surface features. This allows greater contact surface area and better traction on irregular surfaces, and reduce the risk of wheel damage from sharp obstacles.

- **Scalable**: The design should allow scaling and performance prediction for potentially larger diameter deployable tires (> 5m) which may be required depending on the conditions at the landing site and science operations area.

- **Wear resistant**: The wheel must be made of materials that are wear resistant under a range of sharp surface features, under extremely cold temperatures, and must be resistant to high levels of radiation from energetic charged particles on Europa's surface.

- **Traction**: The wheel must allow accommodation of the features on the exterior (such as grousers) to allow sufficient traction for variety of surfaces, obstacles and inclines.

B. Test Tire Design

1. Design Intent

The intent in design of the test tire is two-fold:

1) To support development and validation of a single wheel test rig for Ocean World Rovers, and therefore:
2) To incorporate basic attributes that are functionally relevant to the Ocean World application.

2. Design Concept

The test wheel developed by Thin red Line Aerospace (TRLA) is based on a cutting-edge fabric structure called Ultra High Performance Vessel (UHPV). UHPV was developed by TRLA to address NASA's problem with performance predictability in inflatable structures. TRLA has participated in numerous NASA programs developing mission applications of its patented fabric architecture and validating the predictable scalable performance of its unique structures [47–49].

Ocean Worlds Application

The conceptual design for Ocean World application, as shown in Figure 17, is created by combined utilization of UHPV annulus and oblate spheroid geometries. The exterior tire surface is an unpressurized annulus vessel that is tensioned by a series of interior UHPV oblate spheroids. The configuration is similar to that of ball bearings in a race. The spheroids are also unpressurized, and their radial tendons are tensioned by embedded leaf springs that force the default geometry into place. In addition, a pair of narrow anulus vessels are located within the tire assembly along a circumferential path above and below the spheroids. The narrow annulus vessels are pressured during the deployment process to expand the fabric assembly into its functional geometry. Once deployed, the leaf springs in the oblate spheroids lockup and the tire assembly does not require the outer narrow annulus to be pressurized. However, the smaller diameter inner annulus is required to be pressurized to keep the spokes that form the wheel to be tensioned. This inner annulus is well distanced from the tire tread that remains in contact with the surface. The reliability of the tire can be greatly increased by providing a redundant inner annulus at a very small increase in cost.
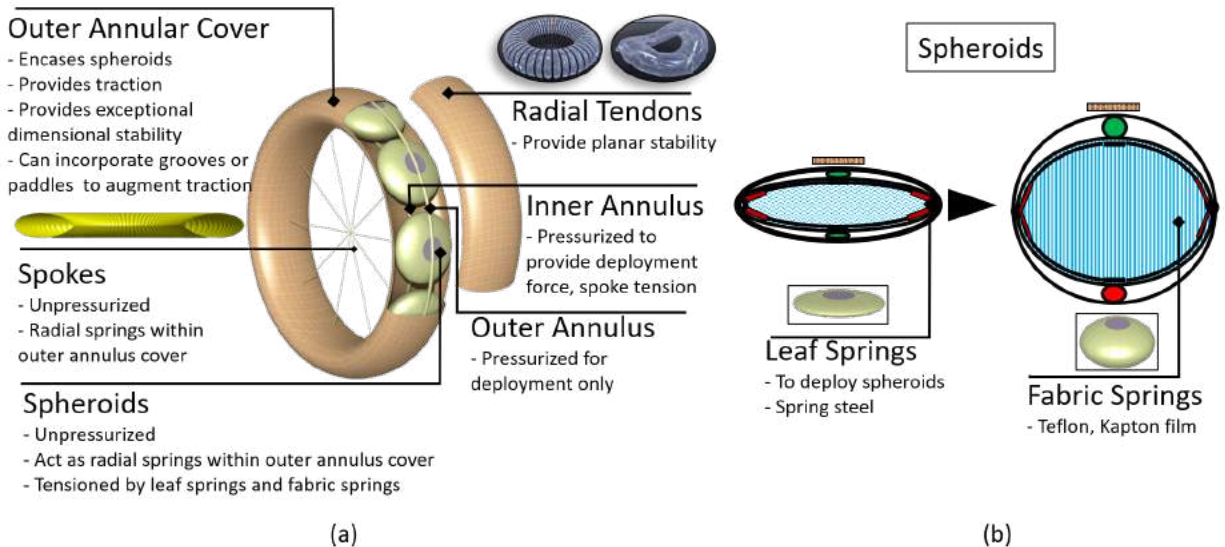

Fig. 17   Conceptual design of the tire. (a) Components of the tire assembly. (b) Cross-section of spheroids.

The resultant configuration is extremely resistant to puncture. It is a lightweight, rugged tire design that conforms to rocky and jagged surfaces which eliminates concentrated contact loads on the tire. The expandable rover tire can be

compactly stowed. The UHPV fabric structure makes it scalable.

Simplified Design for Single Wheel Test Rig Development

In the prototype wheel, the geometry defined in the conceptual design is created using inflatable UHPV oblate spheroids. These spheroids are installed on a metallic rim. An exterior cover is installed to create the effect of the outer annulus cover by enhancing the circularity of the tire's outer mold line. Figure 18 shows rendering of the prototype design.
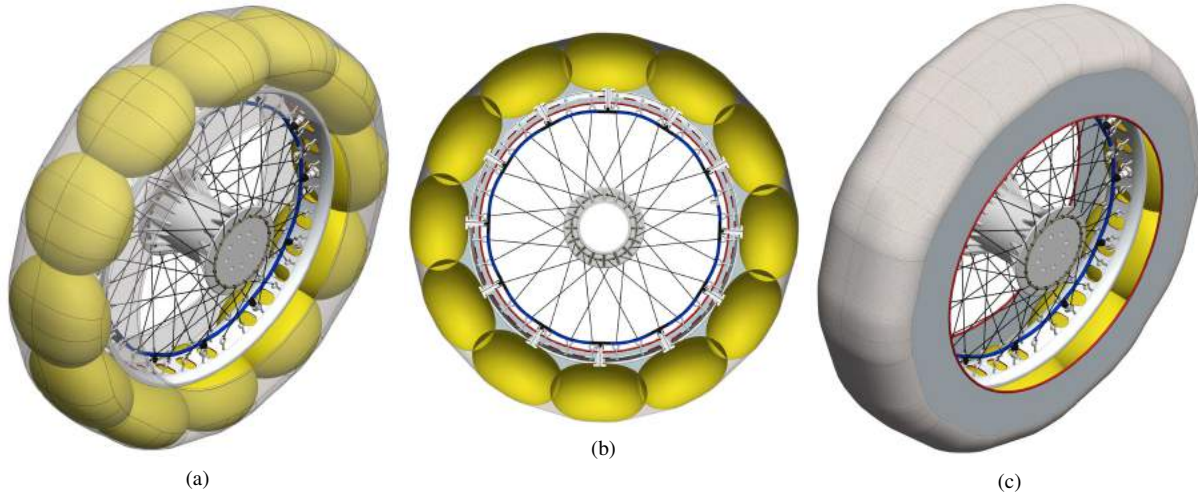

(a)　　　　　　　　(b)　　　　　　　　(c)

Fig. 18　Design rendering of the prototype wheel. (a) Spheroids inside an exterior cover form the tire portion of the wheel and are mounted on a circular metallic ring which is, in turn, connected to the central wheel hub with an array of braided fiber "spokes". (b) Axial view of the tire interior. (c) Tire with the exterior cover.

The fabricated prototype wheel is shown in Figure 19. There are eight inflatable UHPV segments mounted around the outside circumference of a black metallic wheel rim. A central wheel hub facilitates attachment of the wheel assembly to the test rig's axle. Structural concentricity of the hub and rim is provided by an array of 64 flexible Vectran® fiber cordage tendon spokes. An exterior cover is installed over the eight UHPV inflatable segments. The cover reacts the axial distension of the UHPV inflatables (i.e., radially outwards from the wheel center) to enhance the circularity of the tire's outer mold line. All eight yellow inflatable UHPV tire segments are pneumatically manifolded to one-another by means of a circle of clear plastic tubing concentrically positioned between wheel rim and hub.The tread surface of the tire incorporates sixteen sleeves into which tubing stiffeners are inserted to simulate tread-like protrusions.

C. Integration with Test Rig

The tire is mounted on the test rig by attaching the wheel hub to the axle of wheel motor on the rig. Figure 20 shows the mounted tire. A shaft collar is attached to the end of the wheel motor axle. The shaft collar is fitted an adapter to the force and torque sensor, whose other end is attached to another adapter on which the wheel hub is mounted. The adapter between sensor and wheel hub can be modified to mount different wheels. The tire can roll in the surface simulant box along the length of the test rig. The entire wheel drive axle can be tilted along two axes to achieve non-zero slip and
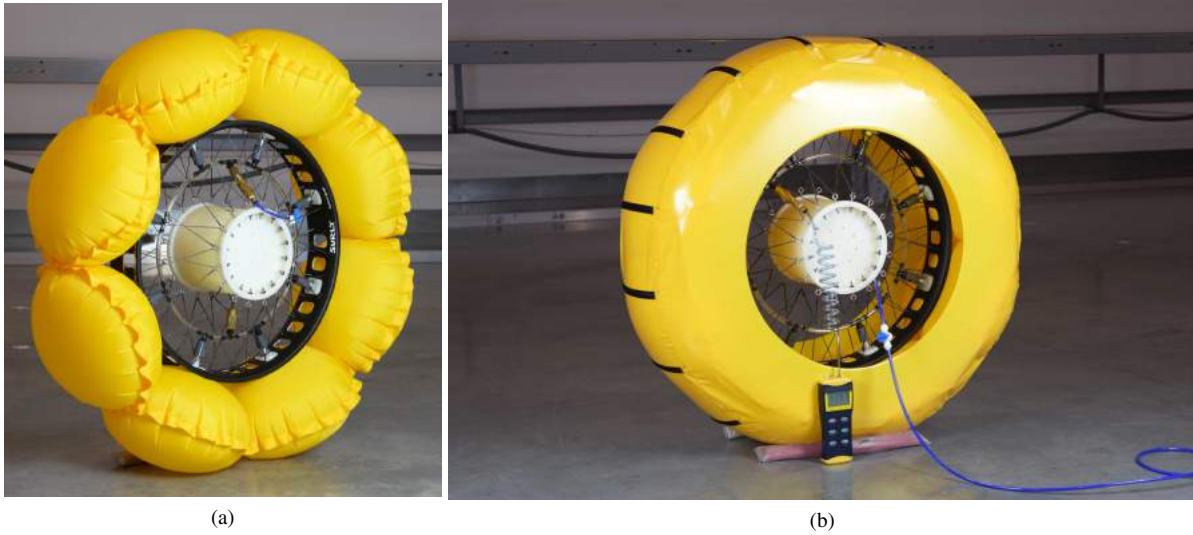
Fig. 19   Fabricated prototype wheel. (a) 8 inflated UHPV spheroids on a black metallic rim and tensioned, braided fiber "spokes". (b) Exterior cover installed over the 8 UHPV inflatable segments.

camber angles.
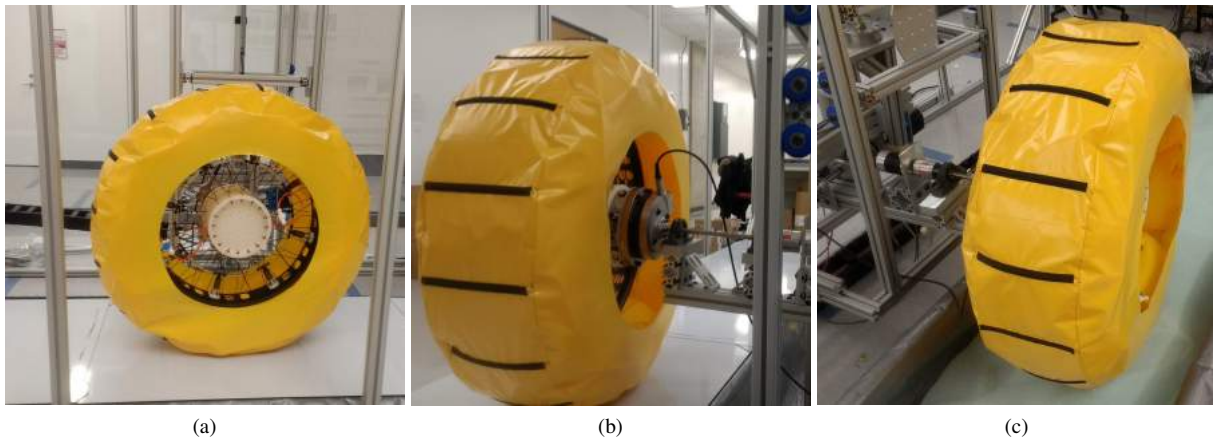
Fig. 20   Prototype tire mounted on test rig. (a) Front view of the inflated tire sitting on a smooth surface. (b) Back view showing the wheel hub assembly attached to the test rig assembly. (c) Side view showing the tire mounted and resting in the surface simulant box.

6. Test Results with Prototype Wheel

A. Validation Effort

A set of experiments were performed at an independent facility to validate the measurements from the single wheel test rig. However, due to incompatibility of the vertical loads on the two test rigs the validation effort could not be completed. Additional details regarding the validation effort are presented in Appendix A.

B. Tests with the Prototype Wheel

To demonstrate the capability of the test rig, a number of tests were performed with various vertical loads, slip ratios, slip angles, and surfaces. Table 2 lists the tests performed in this study. The LabVIEW interface is used to set the parameters, start the test, and record all sensor data at the end of each test.

Table 2   Test cases with prototype wheel

Test no.	Vertical load, N	Slip ratio	Slip angle, deg.	Camber angle, deg.	Surface
1	10	0	0	0	Sandpaper
2	20	0	0	0	Sandpaper
3	30	0	0	0	Sandpaper
4	40	0	0	0	Sandpaper
5	50	0	0	0	Sandpaper
6	10	0.1	0	0	Sandpaper
7	20	0.1	0	0	Sandpaper
8	30	0.1	0	0	Sandpaper
9	40	0.1	0	0	Sandpaper
10	50	0.1	0	0	Sandpaper
11	10	0.2	0	0	Sandpaper
12	20	0.2	0	0	Sandpaper
13	30	0.2	0	0	Sandpaper
14	40	0.2	0	0	Sandpaper
15	50	0.2	0	0	Sandpaper
16	10	0.3	0	0	Sandpaper
17	20	0.3	0	0	Sandpaper
18	30	0.3	0	0	Sandpaper
19	40	0.3	0	0	Sandpaper
20	50	0.3	0	0	Sandpaper

Table 2   Test cases with prototype wheel

Test no.	Vertical load, N	Slip ratio	Slip angle, deg.	Camber angle, deg.	Surface
21	10	0.4	0	0	Sandpaper
22	20	0.4	0	0	Sandpaper
23	30	0.4	0	0	Sandpaper
24	40	0.4	0	0	Sandpaper
25	50	0.4	0	0	Sandpaper
26	10	0.5	0	0	Sandpaper
27	20	0.5	0	0	Sandpaper
28	30	0.5	0	0	Sandpaper
29	40	0.5	0	0	Sandpaper
30	50	0.5	0	0	Sandpaper
31	10	0.6	0	0	Sandpaper
32	20	0.6	0	0	Sandpaper
33	10	0.7	0	0	Sandpaper
34	60	0	0	0	Sandpaper
35	60	0.1	0	0	Sandpaper
36	70	0.1	0	0	Sandpaper
37	10	0	0	0	Glass beads
38	70	0	0	0	Glass Beads
39	50	0	0	0	Glass beads
39	50	0	0	0	Glass beads
40	70	0	0	0	Glass beads
41	10	0.1	0	0	Glass beads
42	30	0.2	0	0	Glass beads
43	50	0.2	0	0	Glass beads

Table 2   Test cases with prototype wheel

Test no.	Vertical load, N	Slip ratio	Slip angle, deg.	Camber angle, deg.	Surface
44	70	0.2	0	0	Glass beads
45	30	0.2	0	0	Glass beads
46	30	0.3	0	0	Glass beads
47	30	0.4	0	0	Glass beads
48	30	0.5	0	0	Glass beads
49	50	0.3	0	0	Glass beads
50	50	0.5	0	0	Glass beads
51	50	0.7	0	0	Glass beads
52	10	0	0	0	Sandpaper
53	20	0	0	0	Sandpaper
54	30	0	0	0	Sandpaper
55	40	0	0	0	Sandpaper
56	50	0	0	0	Sandpaper
57	10	0	10	0	Sandpaper
58	20	0	10	0	Sandpaper
59	30	0	10	0	Sandpaper
60	40	0	10	0	Sandpaper
61	50	0	10	0	Sandpaper
62	10	0	20	0	Sandpaper

C. Data Analysis

The data analysis process consists of filtering, smoothing, and fitting of the sensor data to sinusoidal curves to extract the drawbar pull force, lateral force, and driving torque. Figure 21 shows an overview of the data processing algorithm. The sensor data along with parameters of a single test are recorded in a file. The input parameters for a test include: load, slip ratio, side slip and camber angles. The data corresponding to the FT sensor, load cell, vertical and

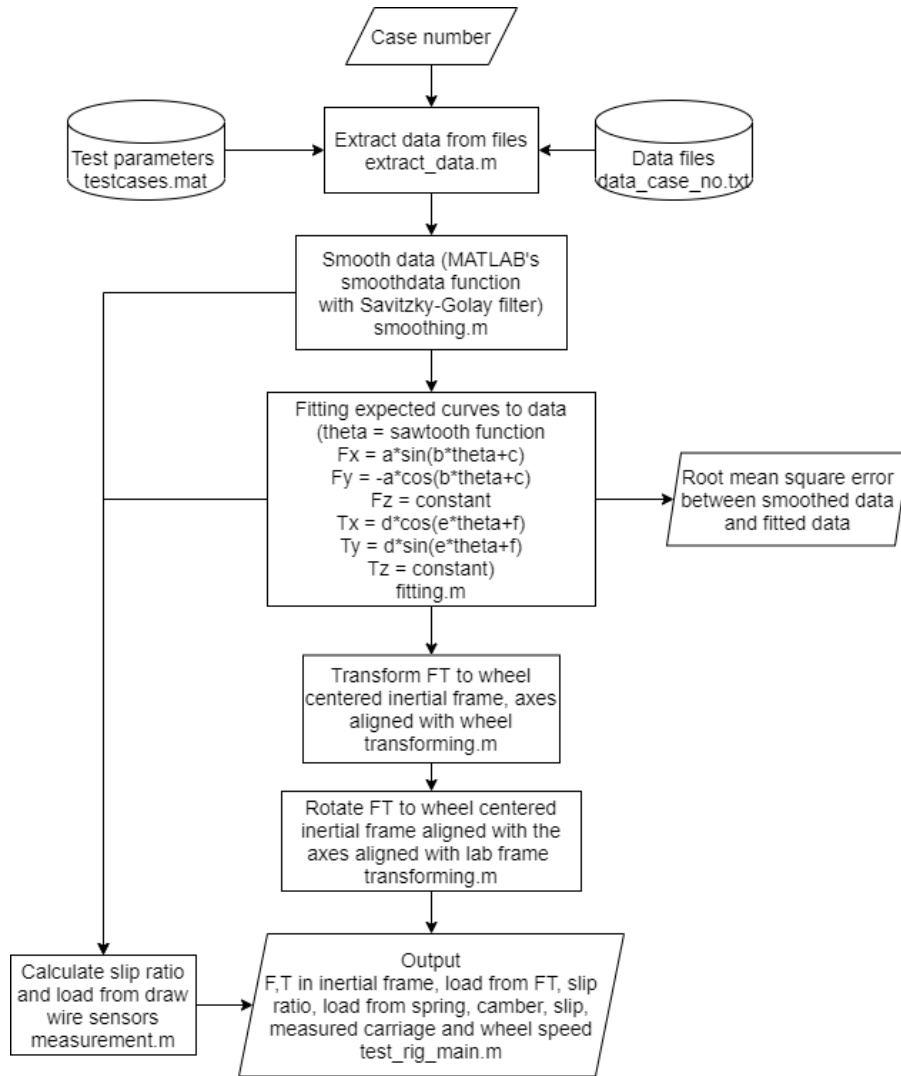horizontal draw wire sensor, inclinometer, and rotary sensor are extracted.

Fig. 21   Data processing algorithm for analysis of sensor data

A filter is applied to smooth the data. The ideal curves are fitted for each type of data. The root mean square for each fit is calculated. The FT sensor is fixed on the wheel and thus gives output in the rotating frame. The FT sensor data is transformed to the inertial frame for the final output. Figure 22 shows plots for FT sensor output data along with the smoothed and fitted data points for Fx and Fy, for the case of 10 N load, zero slip ratio, zero slip and camber angles. A sine and cosine function is fitted for Fx and Fy respectively. The curves have a constant bias that is eliminated when transforming to inertial frame.

D. Tire Test Results

All tests were performed on the prototype wheel with two surfaces: (1) flat surface with sand paper on top, and (2) ocean worlds surface simulant - glass beads. Figure 23 shows drawbar pull force as a function of slip ratio for various
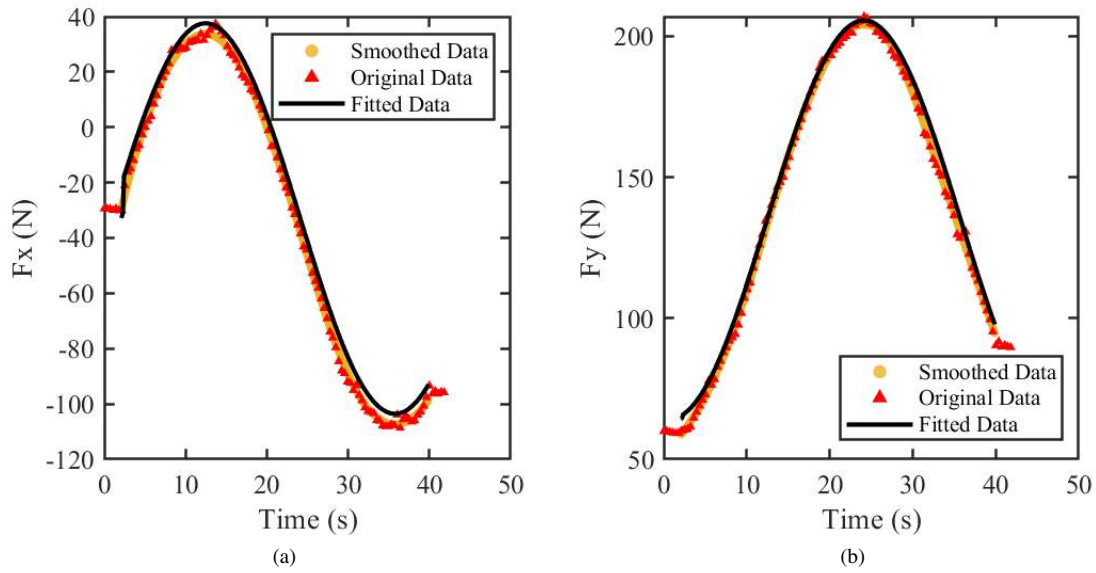
Fig. 22   Data fits for Fx and Fy in the wheel rotating frame.

vertical loads on the two surfaces. The drawbar pull force or traction force, rapidly increases with increasing slip ratio, up to about 0.20. Beyond slip ratio of 0.2, the drawbar pull increases only slightly. The drawbar pull also increases with increasing vertical loads. These trends are qualitatively consistent with other results reported in the literature [50–54].
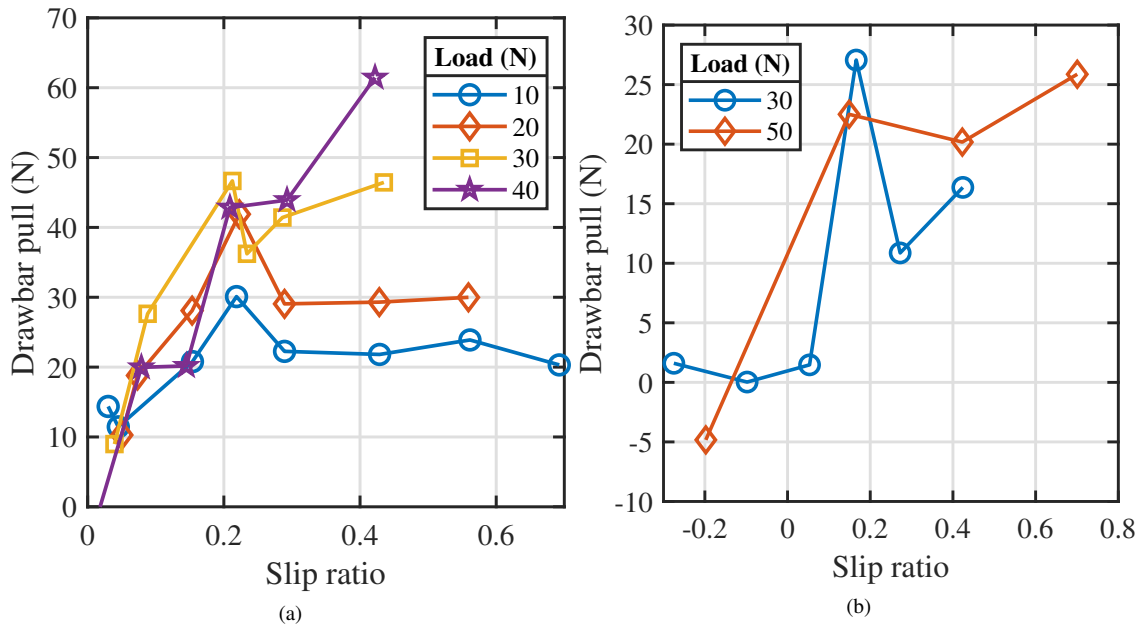

Fig. 23   **Draw bar pull force vs slip ratio for 4 load conditions. (Left) On flat rough surface. (Right) On glass beads surface simulant.**

Figure 24 shows the variation of resistance torque about the wheel rotating axis with slip ratio for various vertical loads. As with the drawbar pull, the torque increases sharply till the slip ratio reaches about 0.20 beyond which it

flattens out. The torque also increases with increasing load, as expected. These trends are also in qualitative agreement with results in the literature [55, 56].
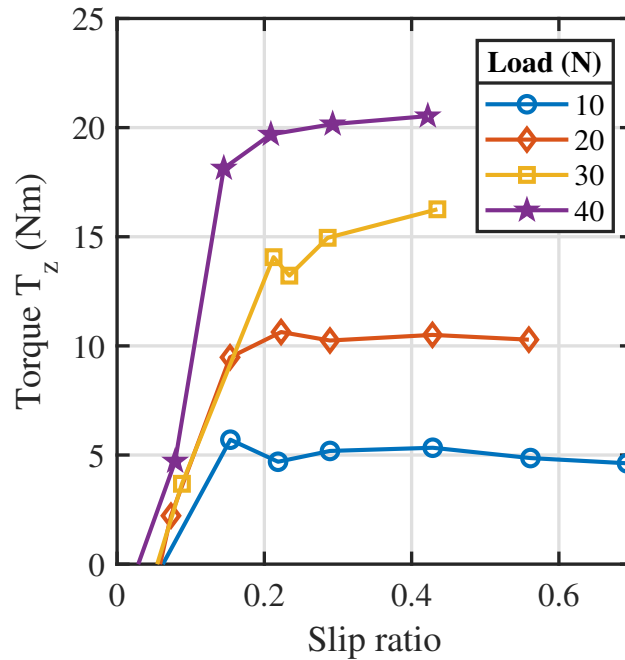

Fig. 24   Torque vs slip ratio for 4 load conditions on a flat rough surface.

Figure 25 shows the lateral force as a function of slip angle for two vertical loads. The lateral force is close to zero for zero side slip which as expected. The small non-zero values are due to asymmetry in the actual wheel and a very small non-zero slip angle due to step control of the motors. The non-zero large lateral force for a 10° slip angle is expected since the wheel rotation axis and direction of traverse are not perpendicular, so the traction force has a component in the perpendicular to that of the traverse direction.

7. Conclusions

A single wheel test rig was developed to study the wheel-terrain interaction of a novel large diameter rover wheel for future Ocean World missions. The test rig allows independent control of the slip ratio, vertical load, slip angle and camber angle. A LabVIEW program has been developed to interface the motors, actuators, and sensors and collect the data. The modular simulant bed allows for a wide range of surfaces to be simulated including flat smooth and rough surfaces, snow, and rock-ice boulder fields. The forces and moments on the wheel, wheel sinkage, and wheel torque are measured by commercial sensors. A 1-meter diameter prototype wheel which incorporates the basic functionality of the proposed large diameter rover wheel has been fabricated and tested. Preliminary results of the drawbar pull, driving torque, and lateral force with the test wheel as a function of slip ratio, vertical load, and slip angle are consistent with those in the literature and demonstrate the basic functionality of the new single wheel Ocean World test rig.
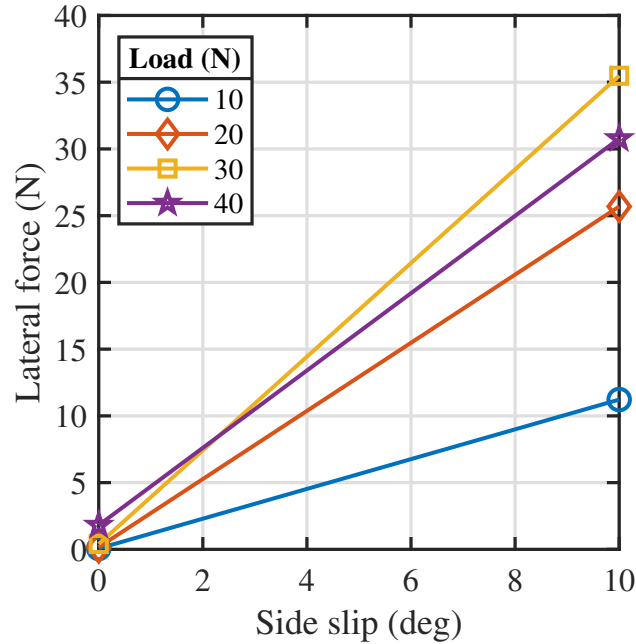
Fig. 25 Lateral force vs side slip angle for various vertical loads on a flat rough surface. The slip ratio is zero.

Appendix A: Validation Testing

A set of experiments were conducted at the Smithers facility automotive tire testing facility in Ravenna, OH to measure the forces and moments on a test wheel under different slip and camber angles. These tests were then replicated at the Purdue facility to validate the test rig results. The objective was to use these measurements to validate the Ocean Worlds test rig sensor measurements. However, two problems were encountered during theses tests: 1) The Smithers facility for terrestrial automotive tire testing is designed for nominal vertical loads of several hundred pounds. The minimum vertical load at which acceptable load control could be achieved was about 100 kg. This implied that the prototype test which was only designed for a load of about 20 kg could not be tested at the Smithers facility. Hence, the Smithers tests were performed with a 16" Dunlop 3402 motorcycle tire at two nominal vertical loads of 90.7 kg and 181.4 kg which were the minimum values at which acceptable load control could be achieved. 2) Attempts to repeat the test with Dunlop tire at the Purdue facility were not successful as the tire was too heavy for the wheel drive structure and no data could be obtained. Figure 28 shows the attempt at testing the motorbike at the test rig.

Figure 26 shows the test bed at Smithers with the major components labeled. The bed consists of a conveyor belt

"road" which is layered with a sandpaper to simulate roughness of a road. The bed can be moved back and forth at varying speeds. The bed is attached to the outer blue frame. The yellow frame holds the wheel, load and camber and slip angle control mechanisms. When the road exerts forces on the wheel, the forces are translated to the yellow frame. There are load cells connecting the yellow frame to the blue frame, which measure the forces exerted on the wheel.
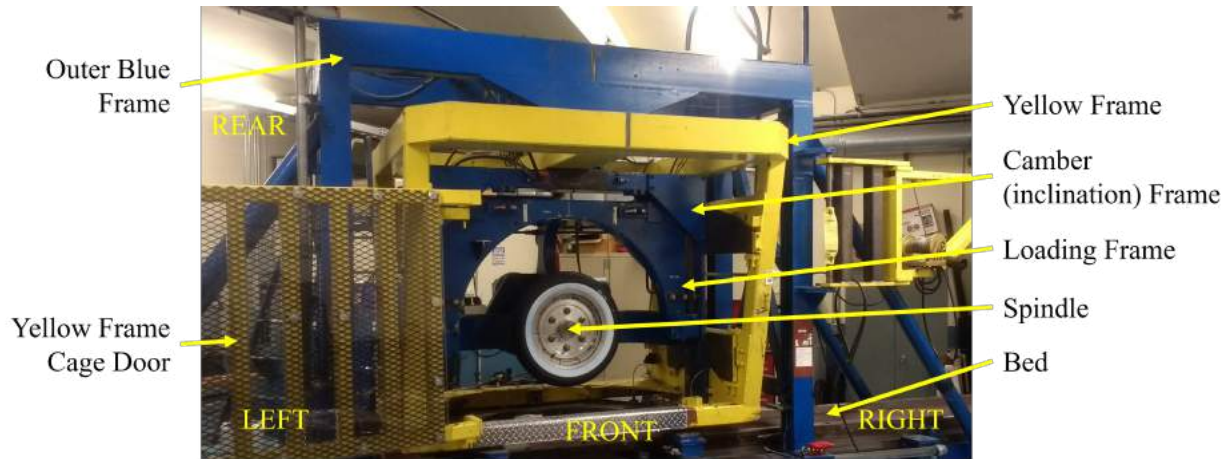
Fig. 26   Test bed at Smithers facility.

The Smithers test rig did not have slip ratio control. Hence, testing is limited to slip and camber angles at two different speeds. Tables 3 and 4 summarize the results from these tests. FX is the longitudinal force or drawbar pull force along the direction of motion of the wheel, FY is the lateral force, and FZ is the normal force. Load is the target load on the tire.

Fig. 27   Testing of the motorbike tire at Smithers facility.

Fig. 28   Validation testing attempt at Purdue facility. The motorbike is shown mounted on the test rig.

Table 3   Test results from Smithers with 3 in/s speed

Camber (deg)	Slip (deg)	FX (kg)	FY (kg)	FZ (kg)	RL (mm)	MX (N-m)	MZ (N-m)	Load (kg)
0	0	-5.47	0	-134	325.4	-7	4	90.7
0	15	0.87	-85	-129	325.1	22	-9	90.7
0	0	-7.11	-1	-221	320.8	7	4	181.4
0	15	4.01	-170	-194	319.0	69	-22	181.4
6	0	-4.38	3	-109	323.3	-237	4	90.7
6	15	0.54	-90	-131	323.6	-201	-9	90.7
6	0	-6.62	13	-198	318.8	-226	7	181.4
6	15	1.39	-174	-197	317.2	-167	-20	181.4

Table 4　Test results from Smithers with 6 in/s speed

Camber (deg)	Slip (deg)	FX (kg)	FY (kg)	FZ (kg)	RL (mm)	MX (N-m)	MZ (N-m)	Load (kg)
0	0	-5.5	0	-134	325.4	-7	4	90.7
0	15	0.9	-85	-129	325.1	22	-9	90.7
0	0	-7.1	-1	-221	320.8	7	4	181.4
0	15	4.0	-170	-194	319.0	69	-22	181.4
6	0	-4.4	3	-109	323.3	-237	4	90.7
6	15	0.5	-90	-131	323.6	-201	-9	90.7
6	0	-6.6	13	-198	318.8	-226	7	181.4
6	15	1.4	-174	-197	317.2	-167	-20	181.4

References

[1] Sanguino, T. d. J. M., "50 years of rovers for planetary exploration: A retrospective review for future directions," *Robotics and Autonomous Systems*, Vol. 94, 2017, pp. 172–185. doi:10.1016/j.robot.2017.04.020.

[2] Kassel, S., "Lunokhod-1 Soviet Lunar Surface Vehicle," Tech. Rep. R-802-ARPA, RAND Corportation, Santa Monica, CA, 1971. URL `https://apps.dtic.mil/dtic/tr/fulltext/u2/733960.pdf`.

[3] Iagnemma, K., and Dubowsky, S., *Mobile robots in rough terrain: Estimation, motion planning, and control with application to planetary rovers*, Vol. 12, Springer Science & Business Media, 2004.

[4] Preumont, A., Alexandre, P., Doroftei, I., and Goffin, F., "A conceptual walking vehicle for planetary exploration," *Mechatronics*, Vol. 7, No. 3, 1997, pp. 287–296. doi:10.1016/S0957-4158(96)00043-8.

[5] Fiorini, P., Hayati, S., Heverly, M., and Gensler, J., "A hopping robot for planetary exploration," *1999 IEEE Aerospace Conference. Proceedings (Cat. No. 99TH8403)*, Vol. 2, IEEE, Aspen, CO, 1999, pp. 153–158. doi:10.1109/AERO.1999.793156.

[6] Balaram, B., Canham, T., Duncan, C., Grip, H. F., Johnson, W., Maki, J., Quon, A., Stern, R., and Zhu, D., "Mars helicopter technology demonstrator," *2018 AIAA Atmospheric Flight Mechanics Conference*, Kissimmee, FL, 2018, p. 0023. doi:10.2514/6.2018-0023.

[7] Hassanalian, M., Rice, D., and Abdelkefi, A., "Evolution of space drones for planetary exploration: A review," *Progress in Aerospace Sciences*, Vol. 97, 2018, pp. 61–105. doi:10.1016/j.paerosci.2018.01.003.

[8] Yajima, N., Izutsu, N., Imamura, T., and Abe, T., *Scientific Ballooning: Technology and applications of exploration balloons floating in the stratosphere and the atmospheres of other planets*, Vol. 112, Springer Science & Business Media, 2009.

[9] Landis, G. A., LaMarre, C., and Colozza, A., "Venus atmospheric exploration by solar aircraft," *Acta Astronautica*, Vol. 56, No. 8, 2005, pp. 750–755. doi:10.1016/j.actaastro.2004.12.001.

[10] Mitri, G., Coustenis, A., Fanchini, G., Hayes, A. G., Iess, L., Khurana, K., Lebreton, J.-P., Lopes, R. M., Lorenz, R. D., Meriggiola, R., et al., "The exploration of Titan with an orbiter and a lake probe," *Planetary and Space Science*, Vol. 104, 2014, pp. 78–92. doi:10.1016/j.pss.2014.07.009.

[11] Weiss, P., Yung, K., Ng, T., Kömle, N., Kargl, G., and Kaufmann, E., "Study of a thermal drill head for the exploration of subsurface planetary ice layers," *Planetary and Space Science*, Vol. 56, No. 9, 2008, pp. 1280–1292. doi:10.1016/j.pss.2008.04.004.

[12] Lorenz, R. D., Oleson, S. R., Colozza, A. J., Jones, R., Packard, T., Hartwig, J., Newman, J. M., Gyekenyesi, J. Z., Schmitz, P., and Walsh, J., "Exploring Titan's cryogenic hydrocarbon seas with boat-deployed expendable dropsondes," *Advances in Space Research*, Vol. 62, No. 4, 2018, pp. 912–920. doi:10.1016/j.asr.2018.05.030.

[13] Welch, R., Limonadi, D., and Manning, R., "Systems engineering the curiosity rover: A retrospective," *2013 8th International Conference on System of Systems Engineering*, IEEE, Maui, HI, 2013, pp. 70–75. doi:10.1109/SYSoSE.2013.6575245.

[14] Williford, K. H., Farley, K. A., Stack, K. M., Allwood, A. C., Beaty, D., Beegle, L. W., Bhartia, R., Brown, A. J., de la Torre Juarez, M., Hamran, S.-E., et al., "The NASA Mars 2020 rover mission and the search for extraterrestrial life," *From Habitability to Life on Mars*, Elsevier, 2018, pp. 275–308. doi:10.1016/B978-0-12-809935-3.00010-4.

[15] Vago, J. L., Westall, F., Coates, A. J., Jaumann, R., Korablev, O., Ciarletti, V., Mitrofanov, I., Josset, J.-L., De Sanctis, M. C., Bibring, J.-P., et al., "Habitability on early Mars and the search for biosignatures with the ExoMars Rover," *Astrobiology*, Vol. 17, No. 6-7, 2017, pp. 471–510.

[16] Ling, Z., Jolliff, B. L., Liu, C., Qiao, L., Cao, H., Zhang, J., Fu, X., Li, B., and Liu, J., "A Close View of Chang'e-4 Landing Site and Science Questions to be Answered by Yutu-2," *50th Lunar and Planetary Science Conference*, Lunar and Planetary Institute The Woodlands, Texas, The Woodlands, TX, 2019.

[17] Lorenz, R. D., and Zimbelman, J. R., "Moving on Sand," *Dune Worlds*, Springer, 2014, pp. 259–272.

[18] Li, R., Wu, B., Di, K., Angelova, A., Arvidson, R. E., Lee, I.-C., Maimone, M., Matthies, L. H., Richer, L., Sullivan, R., et al., "Characterization of traverse slippage experienced by Spirit rover on Husband Hill at Gusev crater," *Journal of Geophysical Research: Planets*, Vol. 113, No. E12, 2008. doi:10.1029/2008JE003097.

[19] Zhou, F., Arvidson, R. E., Bennett, K., Trease, B., Lindemann, R., Bellutta, P., Iagnemma, K., and Senatore, C., "Simulations of mars rover traverses," *Journal of Field Robotics*, Vol. 31, No. 1, 2014, pp. 141–160. doi:10.1002/rob.21483.

[20] Arvidson, R. E., Ashley, J. W., Bell, J., Chojnacki, M., Cohen, J., Economou, T., Farrand, W. H., Fergason, R., Fleischer, I., Geissler, P., et al., "Opportunity Mars Rover mission: Overview and selected results from Purgatory ripple to traverses to Endeavour crater," *Journal of Geophysical Research: Planets*, Vol. 116, No. E7, 2011. doi:10.1029/2010JE003746.

[21] Arvidson, R. E., "Roving on Mars with Opportunity and Curiosity: terramechanics and terrain properties," *Earth and Space 2014*, 2014, pp. 165–173. doi:10.1061/9780784479179.019.

[22] Arvidson, R., DeGrosse Jr, P., Grotzinger, J., Heverly, M., Shechet, J., Moreland, S., Newby, M., Stein, N., Steffy, A., Zhou, F., et al., "Relating geologic units and mobility system kinematics contributing to Curiosity wheel damage at Gale Crater, Mars," *Journal of Terramechanics*, Vol. 73, 2017, pp. 73–93. doi:10.1016/j.jterra.2017.03.001.

[23] Sherwood, B., Lunine, J., Sotin, C., Cwik, T., and Naderi, F., "Program options to explore ocean worlds," *Acta Astronautica*, Vol. 143, 2018, pp. 285–296. doi:10.1016/j.actaastro.2017.11.047.

[24] Nimmo, F., and Pappalardo, R., "Ocean worlds in the outer solar system," *Journal of Geophysical Research: Planets*, Vol. 121, No. 8, 2016, pp. 1378–1399. doi:10.1002/2016JE005081.

[25] Pappalardo, R., Vance, S., Bagenal, F., Bills, B., Blaney, D., Blankenship, D. D., Brinckerhoff, W., Connerney, J., Hand, K., Hoehler, T. M., et al., "Science potential from a Europa lander," *Astrobiology*, Vol. 13, No. 8, 2013, pp. 740–773. doi:10.1089/ast.2013.1003.

[26] Patthoff, D., Meirion-Griffith, G., and Phillips, C., "Science on Europa and Enceladus with a Mobile Platform," *49th Lunar and Planetary Science Conference*, The Woodlands, TX, 2018.

[27] Hand, K. P., et al., *Report of the Europa Lander science definition team*, National Aeronautics and Space Administration, Washington D.C., 2017.

[28] Hobley, D., Moore, J., and Howard, A., "How Rough is the Surface of Europa at Lander Scale?" *44th Lunar and Planetary Science Conference*, The Woodlands, TX, 2013, p. 2432.

[29] Nayar, H., Kim, J., Meirion-Griffith, G., Chamberlain-Simon, B., Carpenter, K., Boettcher, A., Hans, M., and Wilcox, B., "Surface mobility on ocean worlds," *2017 IEEE Aerospace Conference*, IEEE, Big Sky, MT, 2017, pp. 1–10.

[30] Nelson, R. M., Boryta, M. D., Hapke, B. W., Manatt, K. S., Shkuratov, Y., Psarev, V., Vandervoort, K., Kroner, D., Nebedum, A., Vides, C. L., et al., "Laboratory simulations of planetary surfaces: Understanding regolith physical properties from remote photopolarimetric observations," *Icarus*, Vol. 302, 2018, pp. 483–498. doi:10.1016/j.icarus.2017.11.021.

[31] Hobley, D. E., Moore, J. M., Howard, A. D., and Umurhan, O. M., "Formation of metre-scale bladed roughness on Europa's surface by ablation of ice," *Nature Geoscience*, Vol. 11, No. 12, 2018, pp. 901–904. doi:0.1038/s41561-018-0235-0.

[32] Porco, C. C., Helfenstein, P., Thomas, P., Ingersoll, A., Wisdom, J., West, R., Neukum, G., Denk, T., Wagner, R., Roatsch, T., et al., "Cassini observes the active south pole of Enceladus," *science*, Vol. 311, No. 5766, 2006, pp. 1393–1401. doi:10.1126/science.1123013.

[33] Senatore, C., Stein, N., Zhou, F., Bennett, K., Arvidson, R., Trease, B., Lindemann, R., Bellutta, P., Heverly, M., and Iagnemma, K., "Modeling and validation of mobility characteristics of the Mars Science Laboratory Curiosity Rover," *12th International Symposium on Artificial Intelligence, Robotics and Automation in Space (i-SAIRAS)*, Montreal, QC, Canada,, 2014, pp. 17–19.

[34] Moreland, S., Skonieczny, K., Inotsume, H., and Wettergreen, D., "Soil behavior of wheels with grousers for planetary rovers," *2012 IEEE Aerospace Conference*, IEEE, Big Sky, MT, 2012, pp. 1–8. doi:10.1109/AERO.2012.6187040.

[35] Gallina, A., Krenn, R., Scharringhausen, M., Uhl, T., and Schäfer, B., "Parameter identification of a planetary rover wheel–soil contact model via a Bayesian approach," *Journal of Field Robotics*, Vol. 31, No. 1, 2014, pp. 161–175. doi:10.1002/rob.21480.

[36] Ishigami, G., "Terramechanics-based analysis and control for lunar/planetary exploration robots," Ph.D. thesis, Tohuku University, Sendai, Japan, 2008.

[37] Della Torre, A., Finzi, A. E., Genta, G., Curti, F., Schirone, L., Capuano, G., Sacchetti, A., Vukman, I., Mailland, F., Monchieri, E., et al., "AMALIA Mission Lunar Rover—The conceptual design of the Team ITALIA Rover, candidate for the Google Lunar X Prize Challenge," *Acta Astronautica*, Vol. 67, No. 7-8, 2010, pp. 961–978. doi:10.1016/j.actaastro.2010.05.023.

[38] Genta, G., and Pizzamiglio, C., "Testing of planetary rover wheels: Design and setup of a testing machine," *2016 IEEE Metrology for Aerospace (MetroAeroSpace)*, IEEE, Florence, Italy, 2016, pp. 43–48. doi:10.1109/MetroAeroSpace.2016.7573183.

[39] Ding, L., Deng, Z., Gao, H., Nagatani, K., and Yoshida, K., "Planetary rovers' wheel–soil interaction mechanics: new challenges and applications for wheeled mobile robots," *Intelligent Service Robotics*, Vol. 4, No. 1, 2011, pp. 17–38. doi:10.1007/s11370-010-0080-5.

[40] Schäfer, B., Gibbesch, A., Krenn, R., and Rebele, B., "Planetary rover mobility simulation on soft and uneven terrain," *Vehicle System Dynamics*, Vol. 48, No. 1, 2010, pp. 149–169. doi:10.1080/00423110903243224.

[41] Sreenivasulu, S., and Jayalekshmi, S., "Terramechanics on lunar soil simulants: A review," *Int. J. Struct. Civil Eng. Res*, Vol. 3, No. 2, 2014, pp. 92–103.

[42] Ding, L., Deng, Z., Gao, H., Guo, J., Zhang, D., and Iagnemma, K. D., "Experimental study and analysis of the wheels' steering mechanics for planetary exploration wheeled mobile robots moving on deformable terrain," *The International Journal of Robotics Research*, Vol. 32, No. 6, 2013, pp. 712–743. doi:10.1177/0278364912468357.

[43] Moores, J. E., Smith, C. L., Toigo, A. D., and Guzewich, S. D., "Penitentes as the origin of the bladed terrain of Tartarus Dorsa on Pluto," *Nature*, Vol. 541, No. 7636, 2017, pp. 188–190.

[44] Haggart, S., and Waydo, J., "The mobility system wheel design for NASA's Mars Science Laboratory Mission," *11th European Conference of the International Society for Terrain-Vehicle Systems, Torino, Italy*, 2008.

[45] Toupet, O., Biesiadecki, J., Rankin, A., Steffy, A., Meirion-Griffith, G., Levine, D., Schadegg, M., and Maimone, M., "Traction control design and integration onboard the mars science laboratory curiosity rover," *2018 IEEE Aerospace Conference*, IEEE, 2018, pp. 1–20.

[46] Inotsume, H., Moreland, S., Skonieczny, K., and Wettergreen, D., "Parametric study and design guidelines for rigid wheels for planetary rovers," *Journal of Terramechanics*, Vol. 85, 2019, pp. 39–57.

[47] de Jong, M., "Integrated Inflatable Ballute for Planetary Entry, NASA Phase II SBIR Report," Tech. Rep. X9.02-9443, NASA Ames Research Center, 2010.

[48] de Jong, M., "Verification and Validation of Innovative Inflatable Structures Design, NASA Phase II SBIR Report," Tech. Rep. X4.02-9770, NASA Langley Research Center, 2010.

[49] de Jong, M., "Advanced Inflatable Radiation Shielding, NASA Phase I SBIR Report," Tech. Rep. X4.01-8801, NASA Langley Research Center, 2009.

[50] Chunlai, Z., and Mengyan, Z., "Simulation of tire-sand interactions based on FEM/DEM," *Journal of South China University of Technology: Natural Science Edition*, Vol. 43, No. 8, 2015, pp. 75–81. doi:10.1016/j.jterra.2014.05.005.

[51] Yang, F., Sun, W., Lin, G., and Zhang, W., "Prediction of military vehicle's drawbar pull based on an improved relevance vector machine and real vehicle tests," *Sensors*, Vol. 16, No. 3, 2016, p. 351. doi:10.3390/s16030351.

[52] Mousavi, H., and Sandu, C., "Experimental Study of Tread Rubber Compound Effects on Tire Performance on Ice," *SAE International Journal of Commercial Vehicles*, Vol. 13, No. 2, 2020. doi:10.4271/02-13-02-000.

[53] Yoshida, K., Nagatani, K., and Yusa, J., "Traction Performance of Wheel and Track for Soft-Soil Traversal," *International Conference on Robotics and Automation 2010 Planetary Rover Workshop*, 2010.

[54] Zang, M., and Zhao, C., "Numerical simulation of rigid wheel running behavior on sand terrain," *APCOM & ISCM*, Vol. 21, 2013, p. 43.

[55] Liu, J., Gao, H., and Deng, Z., "Effect of straight grousers parameters on motion performance of small rigid wheel on loose sand," *Information Technology Journal*, Vol. 7, No. 8, 2008, pp. 1125–1132.

[56] Kim, K.-J., and Yu, K.-H., "Multidisciplinary Design Optimization for a Solar-Powered Exploration Rover Considering the Restricted Power Requirement," *Energies*, Vol. 13, No. 24, 2020, p. 6652.